

DeepSEE: Deep Disentangled Semantic Explorative Extreme Super-Resolution

Marcel Christoph Bühler, Andrés Romero, and Radu Timofte

Computer Vision Lab, ETH Zürich, Switzerland
{buehlmar, roandres, timofte}@ethz.ch

Abstract. Super-resolution (SR) is by definition ill-posed. There are infinitely many plausible high-resolution variants for a given low-resolution natural image. This is why example-based SR methods study upscaling factors up to $4\times$ (or up to $8\times$ for face hallucination). Most of the current literature aims at a single deterministic solution of either high reconstruction fidelity or photo-realistic perceptual quality. In this work, we propose a novel framework, DeepSEE, for Deep disentangled Semantic Explorative Extreme super-resolution. To the best of our knowledge, DeepSEE is the first method to leverage semantic maps for explorative super-resolution. In particular, it provides control of the semantic regions, their disentangled appearance and it allows a broad range of image manipulations. We validate DeepSEE for up to $32\times$ magnification and exploration of the space of super-resolution.

Keywords: Extreme super-resolution, explorative super-resolution, perceptual super-resolution

1 Introduction

In super-resolution (SR), we learn a mapping G_Θ from a low-resolution (LR) image x_{lr} to a higher-resolution (HR) image \hat{x}_{hr} :

$$\hat{x}_{hr} = G_\Theta(x_{lr}). \quad (1)$$

This mapping can be a standard interpolation method, such as bilinear, bicubic or nearest-neighbour. As such interpolations do not restore high-frequency content or small details, their output is visually clearly different from an original high-resolution image. Consequently, most modern super-resolution methods rely on neural networks to learn a parametrized mapping G_Θ . Such methods usually target upscaling factors of up to $4\times$ in generic domains [41,3], and up to $8\times$ for restricted domains, like faces [54,11,29,9,53,32].

Generic methods lack clear guidance on what characteristics the output images should contain. For example, it is not possible to infer the skin texture from a very low-resolution face image. Solutions for domain-specific methods can include image attributes [54,29,32,30], reference images [31,12] and/or facial landmarks as a guidance [9,11]. Such approaches demonstrate valid results for

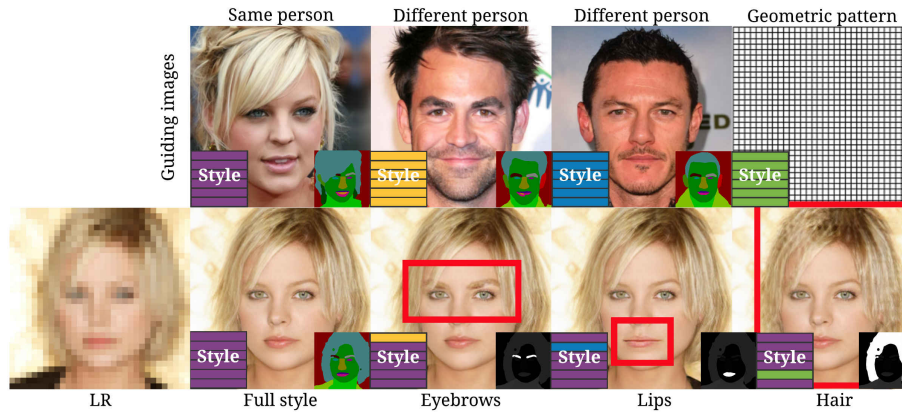


Fig. 1. Upscaling and Manipulations with Disentangled Style Injection. We show multiple outputs for the low-resolution image in the first column. In column two, we apply the full style matrix from an image of the same person. For columns three to five, we extract the style from a guiding image and substitute the rows belonging to the regions that should be adapted. It is even possible to extract a style from geometric patterns, such as the grid in column five. In summary, *DeepSEE* can control the appearance of specific semantic regions



Fig. 2. Multiple Potential Solutions for a Single Input. We upscale a low-resolution image $32\times$ to different high-resolution variants. *Which one would be the correct solution?*

$8\times$ upscaling factors. However, they learn a deterministic mapping and produce a single high-resolution image output for a given input.

Producing a single high-resolution output from a low-resolution image is not ideal, as super-resolution is an ill-posed problem and there are multiple valid solutions for a given input image. Fig. 2 shows a low-resolution input and multiple possible outputs. It is very hard to tell, nonetheless, which image is closest to an unknown ground-truth.

Our proposed method, *DeepSEE*, is capable of generating an infinite number of potentially valid high-resolution candidates for a low-resolution image. The candidates may vary in both appearance and shape, but stay consistent with the low-resolution input. Our method learns a one-to-many mapping from a low-frequency input to a disentangled manifold of potential solutions with the same low-frequencies, but diverse high-frequencies. For inference, a user can tweak the

shape or appearance of individual semantic regions until achieving the desired result.

1.1 Contributions

Our main contributions are as follows:

- i) We introduce *DeepSEE*, a novel framework for **Deep** disentangled **Semantic Explorative Extreme** super-resolution.
- ii) We tackle the ill-posed super-resolution problem in an **explorative** approach based on **semantic maps**. *DeepSEE* is able to sample and manipulate the solution space to produce an infinite number of high-resolution outputs for a single low-resolution input image.
- iii) *DeepSEE* gives control over both shape and appearance. A user can tweak the **disentangled semantic** regions individually.
- iv) We go beyond other approaches by super-resolving to the **extreme**, with upscaling factors up to $32\times$.

2 Related Work

2.1 Classical Super-resolution

Early super-resolution methods were mostly based on edge [14,40] and image statistics [1,55]. Those pre-deep learning techniques relied on paired samples for low and high-resolution images and employed traditional machine learning algorithms, such as support-vector regression [33], graphical models [44], Gaussian process regression [18], sparse coding [50] or piece-wise linear regression [42]. With the advent of deep learning, a multitude of top performing methods were proposed [13,26,41,43], defining the current main stream research in example-based single image super-resolution. Typically, super-resolution aims to restore the missing high-frequencies and details to achieve high (i) **fidelity** or (ii) **perceptual** quality. **Fidelity** quantifies the distortion to a high-resolution ground truth image and **perceptual** metrics measure visual quality. It is important to note that high perceptual quality does not necessarily require a close pixel-wise match to the ground truth (high fidelity).

While most of the research still targets fidelity, the perceptual super-resolution research is starting to bloom. Their results are less blurry and more photo-realistic [3].

Generative Adversarial Networks. Generative Adversarial Networks [15] (GAN) have become increasingly popular in image generation [24,25,34,10,36], thanks to their capability to sample and produce highly realistic images from a target distribution. The underlying technique is to alternately train two convolutional networks, a generator, and a discriminator, with contrary objectives in order to play a MiniMax game. While the discriminator aims to correctly classify whether the images are real or fake, the generator learns to produce photo-realistic images fooling the discriminator.

Perceptual Super-resolution. Super-resolution methods with focus on high fidelity tend to generate blurry images [3]. In contrast, perceptual super-resolution targets photo-realism, but still keeping consistency with the low-frequencies in the input. Please note that high perceptual quality is not necessarily equal to a pixel-wise match to the ground truth (high fidelity). Training perceptual models includes perceptual losses [22], such as those based on the activations of the ImageNet pre-trained VGG-19 network [38], or GANs [27,3,47,5]. A seminal GAN-based work for perceptual super-resolution was SRGAN [27]. SRGAN employed a residual network [19] for the generator and relied on a combination of losses for reconstruction/fidelity, texture/content based on VGG-19 [38] activations, and a GAN discriminator [15] for realism. Follow-up works, such as ESRGAN [47], further improved upon SRGAN by tweaking architecture and loss functions. Recently, [16,17] introduced DIV8K, a dataset of ultra high definition images for extreme super-resolution.

Guided Super-resolution. Super-resolving an image without any additional guidance is a hard problem. This is why many methods condition on previously known or predicted information. Concretely, it is possible to enforce characteristics and guide the image generation via semantic maps [46], attributes [29,32,54,32], facial landmarks [9,11,53], or another image [31,12].

Deterministic Output. One important shortcoming of existing approaches is the deterministic nature of the output, *i.e.* a low-resolution image is mapped to a single output. Such solutions are not ideal, as for a low-resolution image that lacks high-frequency information and details, many potential outputs can resemble the input. In this work, we go in the direction of perceptual super-resolution based on a conditional Generative Adversarial Network that produces highly realistic outputs, and allows for controlling the output in terms of semantic content and appearance.

2.2 Explorative Super-resolution

In super-resolution, many possible solutions for a low-resolution input exist. The possibility to tweak a model’s output is an important step towards making super-resolution even more useful and controllable. In a concurrent work, Bahat *et al.* [2] suggest an editing tool with which a user can manually manipulate the super-resolution output. Their manipulations include adjusting the variance or periodicity (*e.g.* for textures), brightness reduction, or face editing. In our work, do not stop by implementing specific manipulations, but we go further and allow to freely walk a latent style space and explore even more possible solutions. For example, our model can yield face with different skin texture, add/remove lipstick, manipulate eyes, eyebrows, glasses, noses, mouth, *etc.* (Figures 1, 2, 6 and more in the supplementary material). Remarkably, we can either impose different appearance styles per semantic regions from either a latent space or from a reference image. To the best of our knowledge, Bahat *et al.* [2] and our

work are the first works targeting explorative super-resolution and, moreover, *DeepSEE* is the first method that achieves explorative super-resolution using semantically-guided style imposition.

2.3 Domain-specific Super-resolution

Applying super-resolution in a specific domain constrains the problem and improves the quality of the solutions. The focus on a particular domain also makes it easier to leverage prior information. Typical applications include super-resolution of faces [54,11,29,9,53,32], outdoor scenes [46] or depth maps [48,35,21,39]. In this section we focus on super-resolution for faces, namely *face hallucination*.

As faces are very constrained models, there are several ways of supervision that can successfully guide the generation process. Among them, we can find facial keypoints, facial attributes and person identity as three common features. First, influential works [9,53,11] used facial landmarks as heatmaps to align the output with respect to the input, and thus constraint the relative distance of the facial structure in both input and output. Second, other methods [30,29,54] employed binary attributes to enforce the presence or absence of facial components, which preserves the structural consistency in the upscaled image. Lastly, Li *et al.* [31] and Dogan *et al.* [12] leveraged the identity information using the deep features of a facial verification network in order to preserve the perceptual information. Despite the important roles that facial keypoints, attributes and identity preservation play within the facial upscaling, they are a high-level supervision that does not allow fine-grained manipulation of the output, which in most cases, is a desired property.

In contrast to previous works, we use a discrete semantic prior for each region of the face. This allows disentangled manipulations of the semantic layout and style during inference.

2.4 Super-resolution Evaluation

Many standard metrics, such as Peak Signal-to-Noise Ratio (PSNR) or Structural Similarity index [49] (SSIM) evaluate fidelity. However, fidelity does not correlate well with the human visual response of the output [27,3,47,46], *i.e.* a high PSNR or SSIM does not guarantee that the output is perceptually good looking [4]. Alternative metrics, such as the recently proposed LPIPS [56] and FID [20] evaluate perceptual quality. In this work, we emphasize our validation on high perceptual quality as in [27,47,37,46], exploration of the solution space [2] and extreme super-resolution [16].

3 DeepSEE

3.1 Problem Formulation

The low-resolution input ($x_{lr} \in \mathbb{R}^{H_{lr} \times W_{lr} \times 3}$) image acts as a starting point that carries the low-frequency information. The generator (G_{θ}) learns to upscale this

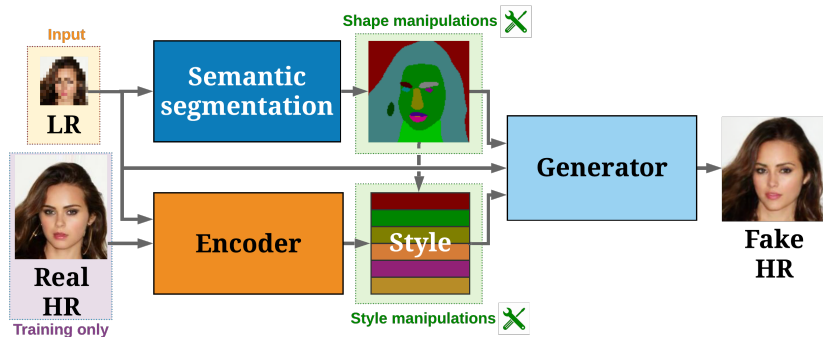


Fig. 3. Overview of *DeepSEE* Components and Data Flow. In addition to the low-resolution image (LR), our generator uses a semantic guidance, as well as a latent representation of style. We train a semantic segmentation network to extract the semantic regions from the low-resolution image. Moreover, a style encoder predicts a region dependent style. During inference, a user can manipulate both semantics and style. For a detailed description, please refer to Section 3 and Fig. 4

image and hallucinates the high-frequencies yielding the high-resolution image $\hat{x}_{hr} \in \mathbb{R}^{H_{hr} \times W_{hr} \times 3}$. As a guidance, G_{Θ} leverages both a high resolution semantic map ($M \in \mathbb{R}^{H_{hr} \times W_{hr} \times N}$, where N is the number of the semantic regions) and independent styles per region ($S \in \mathbb{R}^{N \times d}$, where d is the style dimensionality). The upscaled image should thus retain the low-frequency information from the low-resolution image. In addition, it should be consistent in terms of the semantic regions and have specific, yet independent styles per region. We formally define our problem as

$$\hat{x}_{hr} = G_{\Theta}(x_{lr}, M, S). \quad (2)$$

Remarkably, thanks to the flexible semantic layout, a user is able to control the *appearance* and *shape* of each semantic region through the generation process. This allows to tweak an output until the desired solution has been found.

Following the GAN framework [15], our method consists of a generator and a discriminator network. In addition, we employ a segmentation network and an encoder for style. Concretely, the segmentation network predicts the semantic mask from a low-resolution image and the encoder produces a disentangled style. Fig. 3 illustrates our model at a high level and Fig. 4 provides a more detailed view. In the following, we describe each component in more detail.

3.2 Style Encoder

In- and Outputs. The style encoder E extracts N style vectors of size d from an input image and combines them to a style matrix $S \in \mathbb{R}^{N \times d}$. The style encoder is designed such that it can extract the style from either a low x_{lr} or a high-resolution image x_{hr} . The encoder maps both low and high-resolution

inputs to the same latent style space \mathcal{S} . It disentangles the regional styles via the semantic layout M . The resulting style matrix serves as guidance for the generator.

Architecture. The style encoder consists of a convolutional neural network E^{lr} for the low-resolution and a similar convolutional neural network E^{hr} for the high resolution input. Their output is mapped to the same latent style space via a shared layer E^{Shared} . Fig. 4 illustrates the flow from the inputs to the style matrix. The architecture for the high-resolution input E^{hr} consists of four convolution layers. The input is downsampled twice in the intermediate two layers and upsampled again after a bottleneck. Similarly, the low-resolution encoder E^{lr} consists of four convolution layers. It upsamples the feature map once before the shared layer. The resulting feature map is then passed through the shared convolution layer E^{Shared} and mapped to the range $[-1, 1]$. During inference, a user can sample from this latent space to produce diverse outputs.

Inspired by Zhu *et al.* [57], as a final step, we collapse the output of the shared style encoder for each semantic mask using regional average pooling. This is an important step to disentangle style codes across semantic regions. We describe the regional average pooling in detail in the supplementary material.

3.3 Generator

Our generator learns a mapping $G_{\Theta}(x_{lr}|M, S)$, where the model conditions on both a semantic layout M and a style S . This allows to control the *appearance*, as well as the *size* and *shape* of each region in the semantic layout.

The semantic layout $M \in \{0, 1\}^{H_{hr} \times W_{hr} \times N}$ consists of one binary mask for each semantic region $\{M_0, \dots, M_{N-1}\}$. For style, we assume a uniform distribution $S \in [-1, 1]^{N \times d}$, where each row in S represents a style vector of size d for one semantic region.

At a high level, the generator is a series of residual blocks with upsampling layers in between. Starting from the low-resolution image, it repeatedly doubles the resolution using nearest neighbor interpolation and processes the result in residual blocks. In the residual blocks, we inject semantic and style information through multiple normalization layers. For the semantic layout, we use *spatially adaptive normalization* (SPADE) [34]. SPADE learns a spatial modulation of the feature maps from a semantic map. For the style, we utilize *semantic region adaptive normalization* in a similar fashion as [57]. *Semantic region adaptive normalization* is an extension to SPADE, which includes style. Like SPADE, it computes spatial modulation parameters, but also takes into consideration a style matrix computed from a reference image. In our case, we extract the style S from an input image through our style encoder as described in Section 3.2. For more details, please check the supplementary material.

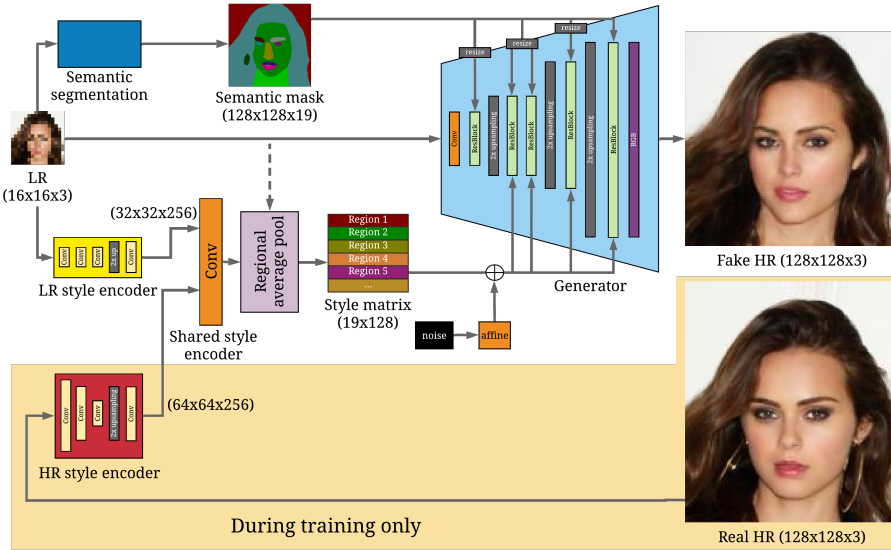


Fig. 4. DeepSEE Architecture. Our Generator upscales a low-resolution image (LR) in a series of residual blocks. A predicted semantic mask guides the geometric layout and a style matrix controls the appearance of semantic regions. The noise added to the style matrix increases the robustness of the model. We describe the style encoding, generator and semantic segmentation in Section 3.2, 3.3, and 3.5, respectively. For more details, please refer to the supplementary material

3.4 Discriminator

We use an ensemble of two similar discriminator networks. One operates on the full image, and the another one on the half-scale of the generated image. Each network takes the concatenation of an image with its corresponding semantic layout and predicts the realism of overlapping image patches. The discriminator architecture follows [34]. Please refer to the supplementary material for a more detailed description.

3.5 Segmentation Network

Our training scheme assumes high-resolution segmentation maps, which in most cases are not available during inference. Therefore, we predict a segmentation map from the low-resolution input image x_{lr} . Particularly, we train a segmentation network to learn the mapping $M = Seg(x_{lr})$, where $M \in \{0, 1\}^{H_{hr} \times W_{hr} \times N}$ is a high-resolution semantic map.

The semantic segmentation network is trained independently from the super-resolution network. For more information, please have a look at the supplementary material.

3.6 DeepSEE Model Variants

We suggest two slightly different variants of our proposed method. The *guided* model learns to super-resolve an image with the help of a high-resolution (HR) reference image. The other (*independent*) model does not require any additional guidance and infers a reference style from the low-resolution image.

The *guided* model is able to apply characteristics from a reference image. When fed a guiding image from the same person, it extracts the original characteristics (if visible). Alternatively, when feeding an image from a different person, it integrates those aspects (as long as it is consistent with the low-resolution input). Figure 1 shows an example, where we first generate an image with the style from the same person and then alter particular regions with styles from other images. The second (*independent*) model applies to the case where no reference image is available.

The *independent* and the *guided* differ in the way how the style matrix S is computed. For the *independent* model, we extract the style from the low-resolution input image: $S = E(x_{lr})$. In contrast, the *guided* model uses a high-resolution reference image x_{hr}^{ref} to compute the style $S = E(x_{hr}^{ref})$. It is worth to mention that for training, paired supervision is not necessary as we only require *one* high resolution picture of a person.

3.7 Training

We train the generator, encoder and discriminator end-to-end in an adversarial setting, similar to [34,45]. As a difference, we inject noise at multiple stages of the generator. We list hyper-parameters and more training details in the supplementary material. In the following, we describe the loss function and explain the noise injection.

Loss Function. Our loss function is identical to [34]. Concretely, our discriminator computes an adversarial loss \mathcal{L}_{adv} with feature matching \mathcal{L}_{feat} . In addition, we employ a perceptual loss \mathcal{L}_{vgg} from a VGG-19 network [38]. Our full loss function is defined in Equation 3:

$$\mathcal{L} = \mathcal{L}_{adv} + \lambda_{feat}\mathcal{L}_{feat} + \lambda_{vgg}\mathcal{L}_{vgg} \quad (3)$$

We set the loss weights to $\lambda_{feat} = \lambda_{vgg} = 10$.

Injection of Noise. After encoding the style to a style matrix S , we add uniformly distributed noise. We define the noisy style matrix S' as $S' = S + U$, where $U \sim Uniform(-\delta, +\delta)$. We empirically choose δ based on the model variant.

Learning Rate. *DeepSEE* needs to handle both low-resolution and high-resolution style inputs. The high-resolution style encoder can extract rich style information. The low-resolution style encoder, however, does not receive such high-frequency information. Therefore, it needs to predict them, which we consider a considerably harder task compared to the high-resolution encoder. Therefore, we set a lower learning rate for the low-resolution style encoder. We train both encoders alternately, by feeding a low-resolution or a high-resolution image in 50% of the iterations. Fig. 4 illustrates the data flow for the style architecture in context of the full *DeepSEE* model. Please refer to the supplementary material for a detailed description of the learning rate and training schedule.

4 Experimental Framework

4.1 Datasets

We train and evaluate our method on face images from CelebAMask-HQ [23,28] and CelebA [32].¹ We use the official training split for developing and training and test on the provided test split. All low-resolution images (serving as inputs) are computed via bicubic downsampling.

4.2 Semantic Segmentation

We train a segmentation network [6,7] on images from CelebAMask-HQ [28,23]. The network learns to predict a high-resolution segmentation map with 19 semantic regions from a low-resolution image. As a model, we choose DeepLab V3+ [6,8,7] with DRN [51,52] as the backbone.

4.3 Baseline

We establish a baseline via bicubic interpolation. We downsample an image to a low-resolution and then upsample back to the original resolution.

4.4 Evaluation Metrics

We compute the traditional super-resolution metrics *peak signal-to-noise ratio* (PSNR), *structural similarity index* (SSIM) [49] and the perceptual metrics *Fréchet Inception Distance* (FID) [20] and *Learned Perceptual Image Patch Similarity* (LPIPS) [56]. Our method focuses on generating results of high perceptual quality, measured by LPIPS and FID. PSNR and SSIM are frequently used, however, they are known not to correlate very well with perceptual quality [56]. However, we still list SSIM scores for completion and report PSNR in the supplementary material.

¹ Our codes and models will be available at: <https://mcbuehler.github.io/DeepSEE/>

Table 1. We list quantitative results on CelebAMask-HQ [28,11] for methods that use a guiding image from the same person. The 32×32 images are upscaled $8\times$. Both our *DeepSEE* variants outperform the other methods on the perceptual metrics (LPIPS [56] and FID [20]). For qualitative results, please refer to the supplementary material

Method	SSIM \uparrow	LPIPS \downarrow	FID \downarrow
Bicubic	0.6635	0.5443	125.148
GFRNet [31]	0.6726	0.3472	55.22
GWAInet [12]	0.6834	0.1832	28.79
ours (independent)	0.6770	0.1691	22.97
ours (guided)	0.6887	0.1519	22.02

5 Discussion

We validate our method on two different setups. First, we compare to state-of-the-art methods in face hallucination and provide both quantitative and qualitative results. Second, we show results for extreme and explorative super-resolution by applying numerous manipulations for upscaling factors of up to $32\times$.

5.1 Comparison to Face Hallucination Methods

To the best of our knowledge, our method is the first face hallucination model based on discrete semantic masks. We compare to models *(i)* that use reference images [31,12] and *(ii)* models guided by facial landmarks [9,11].

For *(i)*, we use the CelebAMask-HQ dataset [23,28] to compare to GFRNet [31] and GWAInet [12], both of which leverage an image from the same person to guide the upscaling. We list quantitative results in Table 1. Our method achieves the best scores for all metrics. For perceptual metrics, LPIPS [56] and FID [20], *DeepSEE* outperforms the other methods by a considerable margin. As we depict in Fig. 5, our proposed method also produces more convincing results, in particular for difficult regions, such as eyes, hair and teeth, our semantic model. We provide more examples in the supplementary material.

For models based on facial landmarks *(ii)*, Table 2 compares to FSRNet [9] and Kim *et al.* [11], where we compute the metrics on the CelebA test set.² *DeepSEE* outperforms FSRNet in all metrics, as well as visually. Please check the supplementary material for a direct visual comparison.

It is important to note that all related face hallucination models output a single solution, *i.e.* for a given input there is always a single output. In fact, however, there exist multiple valid solutions for a low-resolution image. In contrast to prior work, our method can generate an infinite number of solutions, and gives

² The models from [9,11] were trained to generate images of size 128×128 , so we can evaluate in their setting on CelebA. In contrast, the other two related methods [31,12] generate images that are bigger than CelebA [32] (256×256 , whereas CelebA images have size 218×178), hence we evaluate on CelebAMask-HQ [23,28].

Table 2. We compute the scores on the full CelebA test set after center cropping and resizing to 128×128 . The upscaling factor is $8\times$, starting at 16×16 . Our model beats the state-of-the-art in perceptual quality. For a description of our two model variants, please refer to Section 3.6

Method	SSIM \uparrow	LPIPS \downarrow	FID \downarrow
Bicubic	0.5917	0.563	159.60
FSRNet [9] (MSE)	0.5647	0.2885	54.480
FSRNet [9] (GAN)	0.5403	0.2304	55.616
Kim <i>et al.</i> [11]	0.6634	0.1175	11.408
ours (independent)	0.6631	0.1063	13.841
ours (guided)	0.6628	0.1071	11.253

the user fine-grained control over the output. Figures 1 and 2 show several solutions for a low-resolution image. All variants are highly consistent with the low frequencies of the input image. The high-frequencies, however, are not defined by the input and our method generates multiple variants. *DeepSEE* can not only extract the overall appearance from a guiding image of the same person, but it can also inject aspects from other people, and even leverage completely different style images, for instance, geometric patterns. We describe Fig. 1 in more detail in Section 5.2. In addition, our method allows to manipulate semantics, *i.e.* changing the shape, size or content of regions. Figures 1, 2 and 6 illustrate some examples for manipulating eyeglasses, eyebrows, noses, lips, hair, skin, etc. We provide further visualizations in the supplementary material.

5.2 Manipulations

Our proposed approach is an explorative super-resolution model, which allows a user to tune two main *knobs* in order to manipulate the model output. Figure 3 shows these knobs in green boxes.

The first way to change the output image is to adapt the disentangled style matrix, for instance by adding random noise, to interpolate between style codes, or to mix multiple styles, as illustrated by Figure 1. Going from one style code to another gradually changes the image output. For example, manipulating the style code for lips can make them either slowly disappear, or on the contrary, become more prominent. We provide additional examples in the supplementary material.

The second tuning knob is the semantic layout. The user can change the size and shape of semantic regions, which causes the generator to adapt the output representation accordingly. Figure 6 shows an example where we close the mouth and make the chin more pointy by manipulating the regions for lips and facial skin. Furthermore, we change the shape of eyebrows, reduce the nose and update the stroke of the eyebrows. It is also possible to create hair on a bald head or add/remove eyeglasses. Alternatively, a user can change or swap semantic labels.

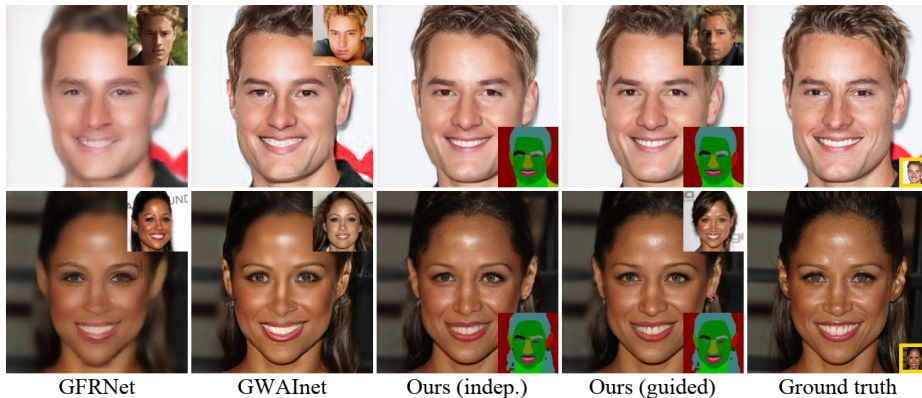


Fig. 5. Comparison to Related Work on $8\times$ Upscaling. We compare to our default solutions for the *independent* and *guided* model settings. The randomly sampled guiding images are on the top right of each image. For *ours*, the bottom right corner shows the predicted semantic mask. Our results are less blurry than GFRNet [31]. Comparing to GWAInet [12], we observe differences in visual quality for difficult regions, like hair, eyes or teeth. With the additional semantic input, our method can produce more realistic textures. Please zoom in for better viewing

We replace eyes with eyebrows and make the nose disappear. We showcase these examples in the supplementary material.

5.3 Extreme Super-resolution

While previous face hallucination models applied upscaling factors of up to $8\times$ [9,12,31,11], *DeepSEE* is capable of going far beyond, with upscaling factors of up to $32\times$. In particular, *DeepSEE* upscales 16×16 low-resolution inputs to 512×512 pixels. This is possible thanks to the conditioning on dense semantic maps, as well as the injection of region-dependent style. Such constraints serve as strict guidance to the generator. As a result, the semantic regions in the super-resolved faces are highly consistent with the input masks and the generated images are of high perceptual quality, even for extreme upscaling factors.

Figure 7 shows results for $32\times$ magnification. For the example on the left, some high-frequency components slightly differ (*e.g.* the exact trimming of the beard, or the wrinkles on the forehead), yet our model captures the main essence and identity from the low-resolution image. The output is highly consistent with the ground truth image (bottom right).

Given such extreme upscaling factors, it is not surprising that we do not always observe such consistent results out of the box. In the second example (Fig. 7 on the right), the upscaled image shows a young woman with a smooth skin texture. In reality, however, the ground-truth image is a middle-aged woman with wrinkles. Wrinkles are a typical example of a high-frequency component that is not clear in a low-resolution image. Most images in CelebAMask-HQ [23,28] show



Fig. 6. Manipulating Semantics. We continuously manipulate the semantic mask and change regional shapes. The first column shows the default solution. For the other columns, we highlight the manipulated regions and show the resulting image. We up-scale with factor $32\times$ and show the input image in the bottom right. For more examples, please refer to the supplementary material

young people with smooth skin. Given the low-resolution version of a middle-aged woman, the style encoder incorrectly inherits the bias of the dataset and predicts the style code of a young woman. This case highlights the benefits of an explorative super-resolution model. With *DeepSEE*, a user is now able to manipulate the style for the skin and generate a solution that matches the ground-truth. Please check the supplementary material for more illustrations and higher-resolution versions of Fig. 7.

6 Ablation Study

We investigate the influence of *DeepSEE*'s main components in an ablation study by training models with the disabled injection of semantics, style, or both. The models are trained for 7 epochs, which corresponds to 3 days on a single TITAN Xp GPU, with upscaling factor $8\times$, batch size 4, and we use the CelebA [32] dataset. More details regarding hyper-parameters can be found in the supplementary material.

6.1 Architectural Differences

For the first model (*Prior-only*), we disable both semantics and style. Therefore, the generator blocks consist of convolutions, batch normalization and ReLU activations. The model's only conditioning is the low-resolution input. For the *hr-guided-only* model, we inject the style matrix computed from another high-resolution image of the same person. Lastly, we train a *semantic-only* model that does not inject any style but applies a semantic layout via spatially adaptive normalization [34].



Fig. 7. Extreme Super-resolution. We show two examples for the upscaling factor $32\times$. The smaller image on each right is the ground truth image from CelebAMask-HQ [23,28]. To illustrate the upscale magnitude, we highlight the low-resolution input image in the bottom left corner in yellow. Please refer to the supplementary material to view these images in high-resolution

Table 3. We conduct an ablation study to compare models with disabled style injection or semantic conditioning. We find that semantics have a strong influence on both fidelity (PSNR and SSIM) and perceptual quality (LPIPS and FID). However, the best scores require both semantics and style. Finally, using a high-resolution guiding image (*guided* model) from the same person provides an additional point of control to the user compared to an *independent* model

Name	Semantics	Style	HR-Guidance	PSNR \uparrow	SSIM \uparrow	LPIPS \downarrow	FID \downarrow
<i>Prior-only</i>	-	-	-	20.883	0.6168	0.123	25.11
<i>Guided-style-only</i>	-	✓	✓	21.564	0.6507	0.111	16.66
<i>Semantics-only</i>	✓	-	-	21.517	0.6543	0.110	12.57
<i>Independent</i>	✓	✓	-	21.852	0.6631	0.106	13.84
<i>Guided</i>	✓	✓	✓	21.726	0.6628	0.107	11.25

6.2 Ablation Discussion

We compare performance scores in Table 3. The performance on all metrics improves when adding either semantics, style or both. Comparing models with either semantics or style (*hr-guided-only* vs. *semantics-only*), the perceptual metrics show better scores when including semantics. In particular, FID [20] is considerably better. Combining both semantic and style yields even better results for both the distortion measures (PSNR and SSIM [49]) and the perceptual metrics (LPIPS [56] and FID [20]). The performance between our two suggested model variants (the *independent* model and *guided* model) is very similar for distortion metrics. In terms of perceptual quality, the *guided* image clearly beats the *independent* in FID. This is not surprising, as it can extract the style from a guiding image of the same person, which makes it easier to produce an image that is close to the ground truth. On the other hand, the *independent* model is more flexible towards random manipulations of the style matrix.

7 Conclusion

The super-resolution problem is ill-posed because a lot of information is missing and needs to be hallucinated. In this paper, we tackle super-resolution in an explorative approach, *DeepSEE*, based on semantic regions and disentangled style codes. *DeepSEE* allows for fine-grained control of the output, disentangled into region-dependent appearance and shape. Our model goes far beyond common upscaling factors ($2\times$ to $8\times$) and allows to magnify up to $32\times$. Our validation for faces demonstrate results of high perceptual quality.

Acknowledgments. This work was partly supported by the ETH Zürich Fund (OK), and by Huawei, Amazon AWS and Nvidia grants.

References

1. Aly, H.A., Dubois, E.: Image up-sampling using total-variation regularization with a new observation model. *IEEE Transactions on Image Processing* **14**(10), 1647–1659 (2005)
2. Bahat, Y., Michaeli, T.: Explorable super resolution. arXiv preprint arXiv:1912.01839 (2019)
3. Blau, Y., Mechrez, R., Timofte, R., Michaeli, T., Zelnik-Manor, L.: The 2018 pirm challenge on perceptual image super-resolution. In: *Proceedings of the European Conference on Computer Vision (ECCV)*. pp. 0–0 (2018)
4. Blau, Y., Michaeli, T.: The perception-distortion tradeoff. In: *Proceedings of the IEEE Conference on Computer Vision and Pattern Recognition*. pp. 6228–6237 (2018)
5. Bulat, A., Tzimiropoulos, G.: Super-fan: Integrated facial landmark localization and super-resolution of real-world low resolution faces in arbitrary poses with gans. In: *Proceedings of the IEEE Conference on Computer Vision and Pattern Recognition*. pp. 109–117 (2018)
6. Chen, L.C., Papandreou, G., Kokkinos, I., Murphy, K., Yuille, A.L.: Deeplab: Semantic image segmentation with deep convolutional nets, atrous convolution, and fully connected crfs. *IEEE transactions on pattern analysis and machine intelligence* **40**(4), 834–848 (2017)
7. Chen, L.C., Papandreou, G., Schroff, F., Adam, H.: Rethinking atrous convolution for semantic image segmentation. arXiv preprint arXiv:1706.05587 (2017)
8. Chen, L.C., Zhu, Y., Papandreou, G., Schroff, F., Adam, H.: Encoder-decoder with atrous separable convolution for semantic image segmentation. In: *Proceedings of the European conference on computer vision (ECCV)*. pp. 801–818 (2018)
9. Chen, Y., Tai, Y., Liu, X., Shen, C., Yang, J.: Fsrnet: End-to-end learning face super-resolution with facial priors. In: *Proceedings of the IEEE Conference on Computer Vision and Pattern Recognition*. pp. 2492–2501 (2018)
10. Choi, Y., Choi, M., Kim, M., Ha, J.W., Kim, S., Choo, J.: Stargan: Unified generative adversarial networks for multi-domain image-to-image translation. In: *Proceedings of the IEEE conference on computer vision and pattern recognition*. pp. 8789–8797 (2018)
11. Deokyun Kim, Minseon Kim, G.K.D.S.K.: Progressive face super-resolution via attention to facial landmark. In: *Proceedings of the 30th British Machine Vision Conference (BMVC)* (2019)

12. Dogan, B., Gu, S., Timofte, R.: Exemplar guided face image super-resolution without facial landmarks. In: Proceedings of the IEEE Conference on Computer Vision and Pattern Recognition Workshops. pp. 0–0 (2019)
13. Dong, C., Loy, C.C., He, K., Tang, X.: Image super-resolution using deep convolutional networks. *IEEE transactions on pattern analysis and machine intelligence* **38**(2), 295–307 (2015)
14. Fattal, R.: Image upsampling via imposed edge statistics. In: ACM SIGGRAPH 2007 papers. pp. 95–es (2007)
15. Goodfellow, I., Pouget-Abadie, J., Mirza, M., Xu, B., Warde-Farley, D., Ozair, S., Courville, A., Bengio, Y.: Generative adversarial nets. In: Advances in neural information processing systems. pp. 2672–2680 (2014)
16. Gu, S., Danelljan, M., Timofte, R., Haris, M., Akita, K., Shakhnarovic, G., Ukita, N., Michelini, P.N., Chen, W., Liu, H., et al.: Aim 2019 challenge on image extreme super-resolution: Methods and results. In: 2019 IEEE/CVF International Conference on Computer Vision Workshop (ICCVW). pp. 3556–3564. IEEE (2019)
17. Gu, S., Lugmayr, A., Danelljan, M., Fritsche, M., Lamour, J., Timofte, R.: Div8k: Diverse 8k resolution image dataset. In: 2019 IEEE/CVF International Conference on Computer Vision Workshop (ICCVW). pp. 3512–3516. IEEE (2019)
18. He, H., Siu, W.C.: Single image super-resolution using gaussian process regression. In: CVPR 2011. pp. 449–456. IEEE (2011)
19. He, K., Zhang, X., Ren, S., Sun, J.: Deep residual learning for image recognition. In: Proceedings of the IEEE conference on computer vision and pattern recognition. pp. 770–778 (2016)
20. Heusel, M., Ramsauer, H., Unterthiner, T., Nessler, B., Hochreiter, S.: Gans trained by a two time-scale update rule converge to a local nash equilibrium. In: Advances in neural information processing systems. pp. 6626–6637 (2017)
21. Hui, T.W., Loy, C.C., Tang, X.: Depth map super-resolution by deep multi-scale guidance. In: European conference on computer vision. pp. 353–369. Springer (2016)
22. Johnson, J., Alahi, A., Fei-Fei, L.: Perceptual losses for real-time style transfer and super-resolution. In: European conference on computer vision. pp. 694–711. Springer (2016)
23. Karras, T., Aila, T., Laine, S., Lehtinen, J.: Progressive growing of gans for improved quality, stability, and variation. arXiv preprint arXiv:1710.10196 (2017)
24. Karras, T., Laine, S., Aila, T.: A style-based generator architecture for generative adversarial networks. In: Proceedings of the IEEE Conference on Computer Vision and Pattern Recognition. pp. 4401–4410 (2019)
25. Karras, T., Laine, S., Aittala, M., Hellsten, J., Lehtinen, J., Aila, T.: Analyzing and improving the image quality of stylegan. arXiv preprint arXiv:1912.04958 (2019)
26. Kim, J., Kwon Lee, J., Mu Lee, K.: Deeply-recursive convolutional network for image super-resolution. In: Proceedings of the IEEE conference on computer vision and pattern recognition. pp. 1637–1645 (2016)
27. Ledig, C., Theis, L., Huszár, F., Caballero, J., Cunningham, A., Acosta, A., Aitken, A., Tejani, A., Totz, J., Wang, Z., et al.: Photo-realistic single image super-resolution using a generative adversarial network. In: Proceedings of the IEEE conference on computer vision and pattern recognition. pp. 4681–4690 (2017)
28. Lee, C.H., Liu, Z., Wu, L., Luo, P.: Maskgan: Towards diverse and interactive facial image manipulation. arXiv preprint arXiv:1907.11922 (2019)
29. Lee, C.H., Zhang, K., Lee, H.C., Cheng, C.W., Hsu, W.: Attribute augmented convolutional neural network for face hallucination. In: Proceedings of the IEEE

- Conference on Computer Vision and Pattern Recognition Workshops. pp. 721–729 (2018)
30. Li, M., Sun, Y., Zhang, Z., Xie, H., Yu, J.: Deep learning face hallucination via attributes transfer and enhancement. In: 2019 IEEE International Conference on Multimedia and Expo (ICME). pp. 604–609. IEEE (2019)
 31. Li, X., Liu, M., Ye, Y., Zuo, W., Lin, L., Yang, R.: Learning warped guidance for blind face restoration. In: Proceedings of the European Conference on Computer Vision (ECCV). pp. 272–289 (2018)
 32. Liu, Z., Luo, P., Wang, X., Tang, X.: Deep learning face attributes in the wild. In: Proceedings of International Conference on Computer Vision (ICCV) (December 2015)
 33. Ni, K.S., Nguyen, T.Q.: Image superresolution using support vector regression. *IEEE Transactions on Image Processing* **16**(6), 1596–1610 (2007)
 34. Park, T., Liu, M.Y., Wang, T.C., Zhu, J.Y.: Semantic image synthesis with spatially-adaptive normalization. In: Proceedings of the IEEE Conference on Computer Vision and Pattern Recognition. pp. 2337–2346 (2019)
 35. Riegler, G., Rüdter, M., Bischof, H.: Atgv-net: Accurate depth super-resolution. In: European conference on computer vision. pp. 268–284. Springer (2016)
 36. Romero, A., Arbeláez, P., Van Gool, L., Timofte, R.: Smit: Stochastic multi-label image-to-image translation. In: Proceedings of the IEEE International Conference on Computer Vision Workshops. pp. 0–0 (2019)
 37. Sajjadi, M.S., Scholkopf, B., Hirsch, M.: Enhancenet: Single image super-resolution through automated texture synthesis. In: Proceedings of the IEEE International Conference on Computer Vision. pp. 4491–4500 (2017)
 38. Simonyan, K., Zisserman, A.: Very deep convolutional networks for large-scale image recognition. *arXiv preprint arXiv:1409.1556* (2014)
 39. Song, X., Dai, Y., Qin, X.: Deep depth super-resolution: Learning depth super-resolution using deep convolutional neural network. In: Asian conference on computer vision. pp. 360–376. Springer (2016)
 40. Sun, J., Xu, Z., Shum, H.Y.: Image super-resolution using gradient profile prior. In: 2008 IEEE Conference on Computer Vision and Pattern Recognition. pp. 1–8. IEEE (2008)
 41. Timofte, R., Agustsson, E., Van Gool, L., Yang, M.H., Zhang, L.: Ntire 2017 challenge on single image super-resolution: Methods and results. In: Proceedings of the IEEE conference on computer vision and pattern recognition workshops. pp. 114–125 (2017)
 42. Timofte, R., De Smet, V., Van Gool, L.: A+: Adjusted anchored neighborhood regression for fast super-resolution. In: Asian conference on computer vision. pp. 111–126. Springer (2014)
 43. Timofte, R., Gu, S., Wu, J., Van Gool, L.: Ntire 2018 challenge on single image super-resolution: Methods and results. In: Proceedings of the IEEE conference on computer vision and pattern recognition workshops. pp. 852–863 (2018)
 44. Wang, Q., Tang, X., Shum, H.: Patch based blind image super resolution. In: Tenth IEEE International Conference on Computer Vision (ICCV’05) Volume 1. vol. 1, pp. 709–716. IEEE (2005)
 45. Wang, T.C., Liu, M.Y., Zhu, J.Y., Tao, A., Kautz, J., Catanzaro, B.: High-resolution image synthesis and semantic manipulation with conditional gans. In: Proceedings of the IEEE conference on computer vision and pattern recognition. pp. 8798–8807 (2018)

46. Wang, X., Yu, K., Dong, C., Change Loy, C.: Recovering realistic texture in image super-resolution by deep spatial feature transform. In: Proceedings of the IEEE conference on computer vision and pattern recognition. pp. 606–615 (2018)
47. Wang, X., Yu, K., Wu, S., Gu, J., Liu, Y., Dong, C., Qiao, Y., Change Loy, C.: Esrgan: Enhanced super-resolution generative adversarial networks. In: Proceedings of the European Conference on Computer Vision (ECCV). pp. 0–0 (2018)
48. Wang, Z., Chen, J., Hoi, S.C.: Deep learning for image super-resolution: A survey. arXiv preprint arXiv:1902.06068 (2019)
49. Wang, Z., Bovik, A.C., Sheikh, H.R., Simoncelli, E.P.: Image quality assessment: from error visibility to structural similarity. *IEEE transactions on image processing* **13**(4), 600–612 (2004)
50. Yang, J., Wright, J., Huang, T.S., Ma, Y.: Image super-resolution via sparse representation. *IEEE transactions on image processing* **19**(11), 2861–2873 (2010)
51. Yu, F., Koltun, V.: Multi-scale context aggregation by dilated convolutions. In: International Conference on Learning Representations (ICLR) (2016)
52. Yu, F., Koltun, V., Funkhouser, T.: Dilated residual networks. In: Computer Vision and Pattern Recognition (CVPR) (2017)
53. Yu, X., Fernando, B., Ghanem, B., Porikli, F., Hartley, R.: Face super-resolution guided by facial component heatmaps. In: Proceedings of the European Conference on Computer Vision (ECCV). pp. 217–233 (2018)
54. Yu, X., Fernando, B., Hartley, R., Porikli, F.: Super-resolving very low-resolution face images with supplementary attributes. In: Proceedings of the IEEE Conference on Computer Vision and Pattern Recognition. pp. 908–917 (2018)
55. Zhang, H., Yang, J., Zhang, Y., Huang, T.S.: Non-local kernel regression for image and video restoration. In: European Conference on Computer Vision. pp. 566–579. Springer (2010)
56. Zhang, R., Isola, P., Efros, A.A., Shechtman, E., Wang, O.: The unreasonable effectiveness of deep features as a perceptual metric. In: CVPR (2018)
57. Zhu, P., Abdal, R., Qin, Y., Wonka, P.: Sean: Image synthesis with semantic region-adaptive normalization. arXiv preprint arXiv:1911.12861 (2019)

DeepSEE: Deep Disentangled Semantic Explorative Extreme Super-Resolution

Supplementary Material

Marcel Christoph Bühler, Andrés Romero, and Radu Timofte

Computer Vision Lab, ETH Zürich, Switzerland
{buehlmar, roandres, timofte}@ethz.ch

1 Architecture

In this section, we describe the *DeepSEE* architecture in more detail. For a clearer understanding, we provide tabular illustrations for the generator and encoder networks for $8\times$ magnification (Tables 4, 1, 2 and 3) and we zoom into the residual blocks where we inject semantic and style information (Fig. 1).

1.1 Style Encoder

The style encoder extracts a style matrix from a low- or high-resolution image. Each row in the style matrix represents a disentangled representation of the appearance of one semantic region. One important step to achieve such a disentanglement is *regional average pooling*. *Regional average pooling* leverages segmentation masks to extract spatial-dependent features.

In our case, it works as follows: The style encoder computes feature maps from an image. We average those features along the spatial dimensions in order to obtain a style matrix $S \in [-1, 1]^{N \times d}$, where N is the number of semantic regions and d is the size of the style vector for one region.

Concretely, let $F \in [-1, 1]^{H_{fm} \times W_{fm} \times d}$ be the encoder features extracted from an image, where H_{fm} and W_{fm} are the output height and width of the shared encoder E^{shared} (described in Section 3.2 in the main paper). For each semantic region, we average the features of that region along the spatial dimensions. First, we scale the predicted binary segmentation mask (Section 3.5 in the main paper) to the size of the feature map: $M^{resized} \in \{0, 1\}^{H_{fm} \times W_{fm} \times N}$. Second, we define the set of all spatial locations belonging to region R_n , $n = 1, \dots, N$ and then compute the entries $k = 1, \dots, d$ in the style matrix S from the features F :

$$R_n = \{(x, y) | M_{x,y,n}^{resized} = 1 \text{ and } x = 1, \dots, H_{fm} \text{ and } y = 1, \dots, W_{fm}\} \quad (1)$$

$$S_{n,k} = \frac{1}{|R_n|} \sum_{(x,y) \in R_n} F_{x,y,k} \quad (2)$$

Table 1. LR Style Encoder Architecture. The low-resolution style encoder consists of a series of convolutional layers with kernel size 3×3 and instance norm layers (IN) [?]. We upsample the feature maps for a better style disentanglement (as described in Section 1.1). The shared style encoder (Table 3) processes the output further and maps it to a shared latent space

Block / Layer	Stride	#Params	Output Shape
Conv+IN	1	864	$16 \times 16 \times 32$
Conv+IN	1	18,432	$16 \times 16 \times 64$
Conv+IN	1	73,728	$16 \times 16 \times 128$
Upsampling	-	0	$32 \times 32 \times 128$
Conv+IN	1	294,912	$32 \times 32 \times 256$
		387,936	

Table 2. HR Style Encoder Architecture. For the high-resolution encoder, we downsample twice and then re-upsample again to create a bottleneck. All convolutions have kernel size 3×3 and they are followed by instance normalization [?]. Again, the shared encoder (Table 3) processes the output further

Block / Layer	Stride	#Params	Output Shape
Conv+IN	1	864	$128 \times 128 \times 32$
Conv+IN	2	18,432	$64 \times 64 \times 64$
Conv+IN	2	73,728	$32 \times 32 \times 128$
Upsampling	-	0	$64 \times 64 \times 128$
Conv+IN	1	294,912	$64 \times 64 \times 256$
		387,936	

1.2 Generator

In this section, we describe the main building block of the generator, the *ResBlock*, and explain how *DeepSEE* injects semantics and style.

Residual Blocks. Starting from a low-resolution image, the generator repeatedly doubles the resolution via nearest-neighbour upscaling and processes the result in residual blocks (ResBlocks). As a guidance, the ResBlocks inject semantic and style information via spatially adaptive normalization (SPADE) [34] and *semantic region adaptive normalization* [57].

Figure 1 shows a ResBlock and zooms into the normalization block (NormBlock). The ResBlock follows the design by [57] and processes the input feature maps with two normalization blocks NormBlocks in a main path and one NormBlock in a residual connection. It also adds noise from a standard normal distribution, which improved the FID score in [57].

The NormBlock (Fig. 1) learns two sets of modulation parameters. The first set is responsible for semantic consistency. The second set applies the disen-

Table 3. Shared Style Encoder Architecture. The shared style encoder processes the output of both the low-resolution and the high-resolution encoders and maps their outputs to a latent space. It uses a predicted semantic mask to extract styles for each semantic region in the regional average pooling layer. For a detailed description of regional average pooling, please refer to Section 1.1

Block / Layer	Stride	#Params	Output Shape LR	Output Shape HR
Conv+IN	1	294,912	$32 \times 32 \times 128$	$64 \times 64 \times 128$
Tanh	-	0	$32 \times 32 \times 128$	$64 \times 64 \times 128$
Regional avg pool	-	0	19×128	19×128
		294,912		

Table 4. Generator Architecture for $8\times$ Magnification. We list the main layers and building blocks with the number of parameters and output shapes. All residual blocks inject semantics [34] and style [57], except for the first residual block, which only injects semantics. Please refer to Fig. 1 for a detailed view of the ResBlock

Block / Layer	Semantics	Style	#Params	Output Shape
Conv	-	-	14,336	$16 \times 16 \times 512$
ResBlock	✓	-	7,126,528	$16 \times 16 \times 512$
Upsampling	-	-	0	$32 \times 32 \times 512$
ResBlock	✓	✓	9,488,636	$32 \times 32 \times 512$
ResBlock	✓	✓	9,488,636	$32 \times 32 \times 512$
Upsampling	-	-	0	$64 \times 64 \times 512$
ResBlock	✓	✓	9,488,636	$64 \times 64 \times 512$
Upsampling	-	-	0	$128 \times 128 \times 512$
ResBlock	✓	✓	9,488,636	$128 \times 128 \times 512$
Conv	-	-	13,827	$128 \times 128 \times 3$
Tanh	-	-	0	$128 \times 128 \times 3$
			45,109,235	

tangled style information from a style matrix. As a reminder, the style matrix contains a style vector for each semantic region. For computing the modulation parameters, the style matrix expands and colors the semantic mask, yielding a *styled map*. Similar to previous work [34,57], we compute a scale and offset for each feature pixel. As a last step, we combine the two sets of modulation parameters via a weighted average and apply them to the input feature map. In our ablation study (in the main paper), we compare the model performance for variants where we remove semantics, style or both from the NormBlock.

Upsampling and Number of Layers. The generator consists of residual blocks, which refine the output of deterministic upscaling layers. The number of upscaling layers depends on the magnification factor. Each upscaling layer increase the image dimensions by the factor 2. For upscaling $4\times$, our model

consists of 2 upscaling layers. A model with upscaling factor 2^i applies i upscaling layers. For example, our extreme super-resolution model with upscaling factor $32 = 2^5$ consists of 5 upscaling layers.

1.3 Discriminator

Our Patch-GAN discriminator [?] follows the one in [34]. It consists of two networks, one that operates on the high-resolution image and one on the half scale. The networks take the concatenation of an image together with its segmentation mask as input. Both networks predict the realism of overlapping image patches and the loss function computes the average Hinge loss of their outputs.

Architecturally, four convolutional and spectral instance normalization [?] layers process the input, with leaky ReLU [?, ?, ?] as the activation function. In the first three layers, we use a stride of two in order to reduce the feature map size. The last convolution applies a stride of one. We use the same number of discriminator layers for all our experiments.

1.4 Semantic Segmentation Network

We train a state-of-the-art DeepLab semantic segmentation network [6,7] to predict a high-resolution segmentation map $M \in \{0, 1\}^{H_{hr} \times W_{hr} \times N}$ from a low-resolution image $x_{lr} \in \mathbb{R}^{H_{lr} \times W_{lr} \times 3}$. Our segmentation model first upscales the low-resolution image to the high-resolution and then processes it in the same way as a regular high-resolution image.

We train the segmentation model on the CelebAMask-HQ [28,23] dataset for 150 epochs, with a polynomially decaying learning rate of 0.001 and stochastic gradient descent with momentum 0.9 and weight decay 0.0005.

Table 5 lists performance metrics with different backbones. All of the models are trained with balanced class weights. For our experiments, we choose the best scoring model with DRN backbone [51,52]. Figure 2 shows a random sample of qualitative results.

2 Training and Testing

In this section, we list training details and hyper-parameters and describe the test dataset splits. Unless otherwise stated, we use the same hyper-parameters for all our experiments.

2.1 Training Details

Optimizer and Learning Rate. In all our super-resolution experiments, we use the Adam [?] optimizer. We set the parameters for the exponentially moving average as $\beta_1 = 0.0$ and $\beta_2 = 0.9$ for the squared gradient. We chose the learning rate 0.0001 for the generator and 0.0004 for the discriminator. The high-resolution and the shared style encoders have the same learning rate as the generator. The low-resolution style encoder is trained with a smaller learning rate of 0.000025.

Initialization. We initialize all our networks using xavier [?] with a variance of 0.02.

Training Time. On CelebA [32], a large dataset with 162,770 training samples, we train for 8 epochs, linearly decaying the learning rate in the last 3 epochs. On CelebAMask-HQ [28,23], whose train split consists of 24,183 samples, we train for 75 epochs in total, and linearly decay the learning rate in the last 25 epochs. The training time is between 3-5 days on a TITAN Xp GPU on both datasets for $8\times$ magnification. For the extreme upscaling factors ($32\times$), training takes between 7-8 days on 2 Tesla V100 GPUs.

Batch Size. We vary batch size according to the input image size and upscaling factors. For experiments starting at 16×16 low-resolution images and magnification factor $8\times$, we set the batch size to 4. For the experiments that upscale 32×32 images, we reduce the batch size to 1. Similarly, we use batch size 1 for all experiments with extreme upscaling factors ($32\times$).

Noise Injection. We inject uniformly distributed noise into the style matrix to increase the model’s robustness towards exploration of the style space, as described in Section 3.7 in the main paper. The scale of the noise depends on the model variant. For the *independent* model, we choose $\delta = 0.2$. The *guided* model is trained with $\delta = 0.05$.

2.2 Testing

Datasets. We compute the following test scores for all datasets on the official test splits [32,28,23]: PSNR, SSIM [49], LPIPS [56] and FID [20]. For CelebA, the test dataset consists of 19,962 samples. The CelebAMask-HQ test set contains 2,824 samples. For CelebA, the predicted segmentation masks are of size 128×128 , and for CelebAMask-HQ, we predict high-resolution segmentation masks of size 512×512 .

Our *guided* model, as well as some of the related work [31,12] require an additional guiding image from the same person. For those experiments, we omit people who only appear once in the dataset.

Pre-processing. For our models, we calculate the low-resolution input via bicubic interpolation. For the related work, we follow their pre-processing and use their respective downsampling method as input to their models.

The CelebA [32] images have height 218 and width 178 pixels. We center crop the CelebA images to 178×178 pixels and resize them to 128×128 for the high-resolution ground truth.

For CelebAMask-HQ [28,23], we resize the images to the desired high-resolution (512×512 for the extreme super-resolution and 256×256 for comparing to [31,12]).

Table 5. Results for Semantic Segmentation on Low-resolution Images. The segmentation network predicts 128×128 segmentation masks from 16×16 images. We report accuracy (Acc), mean Intersection-over-Union (mIoU) and frequency-weighted Intersection-over-Union (fwIoU)

Backbone	Acc \uparrow	mIoU \uparrow	fwIoU \uparrow
Xception [?]	0.821	0.457	0.714
Resnet [?]	0.848	0.457	0.747
DRN [51,52]	0.877	0.547	0.794

3 Additional Results

3.1 Exploration of the Solution Space

DeepSEE is able to sample in the manifold of possible solution for a given low-resolution image. This can be very useful in a broad range of scenarios. For example, some applications might be more interested in high fidelity, while others need images of high perceptual quality. To illustrate the dynamic nature of *DeepSEE*, we take 12 random images and sample 1,000 different potential solutions for each of them. The plots in Figures 5 and 6 show the resulting scores for fidelity (SSIM [49], y-axis) and perceptual quality (LPIPS [56], x-axis).

In theory, one could sample an infinite number of times to increase the chances of producing the desired result. However, in most cases, a relatively small sample of 10 already contains sufficient variability. To illustrate the impact of sampling upscaled variants on the fidelity and perception metrics, we sample 1, 10, 100 and 1,000 random solutions and mark the best-scoring sample in terms of SSIM (Figure 6) and LPIPS (Figure 5). We conclude that *DeepSEE* can obtain high scoring solutions for both objectives: high fidelity and perceptual quality.

3.2 Semantic Manipulations

We provide additional semantic manipulations on images with upscaling factor $32\times$. Figure 7 demonstrates multiple manipulations for the same sample. In the group, we first close the eyes and reopen them again. For the last two versions, we slightly open the mouth and remove the glasses. For the second example, we play with the mouth and hair. It is interesting to note that despite the large added hair region (light blue in the last two columns), the model produces relatively little hair. This is most likely due to the low-resolution prior, which does not have hair in that region. In the last example, we close the mouth in multiple steps for a smooth transition.

In Fig. 8, we replace the teeth region with lips in the top row and in the second row, we remove the eyebrows. In the third row, we remove the annotations for the large hair region. One might expect the model to produce a bold head,

but instead we get a head with smooth hair. The reason for this is again the conditioning on the low-resolution input. The low-resolution image indicates the presence of a dark region, which is in contrast to a bright bold head. Hence, the model decides to create some smooth hair, despite the missing annotation in the semantic input. In the last row, we remove the annotations for eye glasses. Remarkably, *DeepSEE* interprets the dark pixels from the low-resolution input as strong makeup.

In summary, *DeepSEE* allows a broad range of semantic manipulations, as long as they are roughly consistent with the low-resolution input.

3.3 Influence of Gradual Changes in the Style Matrix

We provide additional results for the *independent* model, where we walk in the latent style space. Figure 3 and 4 show results for the *independent* model. We predict the style matrix from a low-resolution image (column two) and produce multiple gradually varying solutions. The middle image (column five) is generated via the unmodified predicted style from the low-resolution image. The images to the left (columns three and four) are generated after subtracting a δ from the original style matrix. Similarly, we generate the images on the right (columns six and seven) by adding a δ to the style matrix. As a result, we observe that larger values in the style matrix (columns six and seven) tend to yield more contrast and darker colors, in particular for lips, eyes and eyebrows. Contrary, smaller values in the style matrix (columns three and four) produce a rather bleached out image.

3.4 Disentangled Manipulations

In above section (Section 3.3), we modified the full style matrix. Now, in Figure 9, we only manipulate some specific rows in the style matrix. This limits the changes to the corresponding semantic region. For example, the first two rows show the same output face, but with changes in the hair style. The changes in row three and four are limited to the skin area. Please zoom in to see differences in skin texture. Similarly, the rows five to seven manipulate a single semantic region only (lips, eyebrows and eyes).

3.5 Visualizations of Extreme Super-resolution

Figures 13 and 14 visualize the extreme super-resolution examples from the main paper in higher resolution and Fig. 15 shows one additional example.

4 Additional Comparisons

We extend our quantitative comparison to related work in Tables 6 and 7. The former extends Table 1 from the main paper, the latter adds to Table 2 from the main paper. Qualitatively, we add more examples for GFRNet [31] and

Table 6. Extended Quantitative Evaluation on CelebA. We copy Table 1 from the main paper and add PSNR. The scores are computed on the full test set after center cropping and resizing to 128×128 and the upscaling factor is $8\times$, starting at 16×16

Method	PSNR \uparrow	SSIM \uparrow	LPIPS \downarrow	FID \downarrow
Bicubic	20.67	0.5917	0.5625	159.60
FSRNet [9] (MSE)	20.03	0.5647	0.2885	54.480
FSRNet [9] (GAN)	19.75	0.5403	0.2304	55.616
Kim <i>et al.</i> [11]	23.29	0.6634	0.1175	11.408
ours (independent)	21.85	0.6631	0.1063	13.841
ours (guided)	21.73	0.6628	0.1072	11.253

Table 7. Extended Quantitative Evaluation on CelebAMask-HQ. We copy Table 2 from the main paper and add PSNR. We compare to models that require a guiding image from the same person. The 32×32 face images are upscaled $8\times$

Method	PSNR \uparrow	SSIM \uparrow	LPIPS \downarrow	FID \downarrow
Bicubic	23.13	0.6635	0.5443	125.148
GFRNet [31]	24.69	0.6726	0.3472	55.22
GWAINet [12]	24.81	0.6834	0.1832	28.79
ours (<i>independent</i>)	23.54	0.6770	0.1691	22.97
ours (<i>guided</i>)	23.94	0.6887	0.1519	22.02

GWAINet [12] in Figures 10 and 11. Finally, we provide a visual comparison to methods based on facial landmarks [11,9] in Fig. 12. Comparing to Kim *et al.*, our models achieve better results for perceptual metrics. Qualitatively, their outputs struggle with texture and shape of the more difficult areas, like hair or teeth. This outcome is not surprising because their face alignment ignores out-of-face regions, and without guidance, it is much more difficult to learn concepts that only cover a small area, as in the mouth region. In contrast, our method benefits from knowledge about semantic regions, which allows for guidance beyond facial landmarks.

References

1. Aly, H.A., Dubois, E.: Image up-sampling using total-variation regularization with a new observation model. *IEEE Transactions on Image Processing* **14**(10), 1647–1659 (2005)
2. Bahat, Y., Michaeli, T.: Explorable super resolution. *arXiv preprint arXiv:1912.01839* (2019)
3. Blau, Y., Mechrez, R., Timofte, R., Michaeli, T., Zelnik-Manor, L.: The 2018 pirm challenge on perceptual image super-resolution. In: *Proceedings of the European Conference on Computer Vision (ECCV)*. pp. 0–0 (2018)

4. Blau, Y., Michaeli, T.: The perception-distortion tradeoff. In: Proceedings of the IEEE Conference on Computer Vision and Pattern Recognition. pp. 6228–6237 (2018)
5. Bulat, A., Tzimiropoulos, G.: Super-fan: Integrated facial landmark localization and super-resolution of real-world low resolution faces in arbitrary poses with gans. In: Proceedings of the IEEE Conference on Computer Vision and Pattern Recognition. pp. 109–117 (2018)
6. Chen, L.C., Papandreou, G., Kokkinos, I., Murphy, K., Yuille, A.L.: Deeplab: Semantic image segmentation with deep convolutional nets, atrous convolution, and fully connected crfs. *IEEE transactions on pattern analysis and machine intelligence* **40**(4), 834–848 (2017)
7. Chen, L.C., Papandreou, G., Schroff, F., Adam, H.: Rethinking atrous convolution for semantic image segmentation. *arXiv preprint arXiv:1706.05587* (2017)
8. Chen, L.C., Zhu, Y., Papandreou, G., Schroff, F., Adam, H.: Encoder-decoder with atrous separable convolution for semantic image segmentation. In: Proceedings of the European conference on computer vision (ECCV). pp. 801–818 (2018)
9. Chen, Y., Tai, Y., Liu, X., Shen, C., Yang, J.: Fsrnet: End-to-end learning face super-resolution with facial priors. In: Proceedings of the IEEE Conference on Computer Vision and Pattern Recognition. pp. 2492–2501 (2018)
10. Choi, Y., Choi, M., Kim, M., Ha, J.W., Kim, S., Choo, J.: Stargan: Unified generative adversarial networks for multi-domain image-to-image translation. In: Proceedings of the IEEE conference on computer vision and pattern recognition. pp. 8789–8797 (2018)
11. Deokyun Kim, Minseon Kim, G.K.D.S.K.: Progressive face super-resolution via attention to facial landmark. In: Proceedings of the 30th British Machine Vision Conference (BMVC) (2019)
12. Dogan, B., Gu, S., Timofte, R.: Exemplar guided face image super-resolution without facial landmarks. In: Proceedings of the IEEE Conference on Computer Vision and Pattern Recognition Workshops. pp. 0–0 (2019)
13. Dong, C., Loy, C.C., He, K., Tang, X.: Image super-resolution using deep convolutional networks. *IEEE transactions on pattern analysis and machine intelligence* **38**(2), 295–307 (2015)
14. Fattal, R.: Image upsampling via imposed edge statistics. In: ACM SIGGRAPH 2007 papers. pp. 95–es (2007)
15. Goodfellow, I., Pouget-Abadie, J., Mirza, M., Xu, B., Warde-Farley, D., Ozair, S., Courville, A., Bengio, Y.: Generative adversarial nets. In: Advances in neural information processing systems. pp. 2672–2680 (2014)
16. Gu, S., Danelljan, M., Timofte, R., Haris, M., Akita, K., Shakhnarovic, G., Ukita, N., Michelini, P.N., Chen, W., Liu, H., et al.: Aim 2019 challenge on image extreme super-resolution: Methods and results. In: 2019 IEEE/CVF International Conference on Computer Vision Workshop (ICCVW). pp. 3556–3564. IEEE (2019)
17. Gu, S., Lugmayr, A., Danelljan, M., Fritsche, M., Lamour, J., Timofte, R.: Div8k: Diverse 8k resolution image dataset. In: 2019 IEEE/CVF International Conference on Computer Vision Workshop (ICCVW). pp. 3512–3516. IEEE (2019)
18. He, H., Siu, W.C.: Single image super-resolution using gaussian process regression. In: CVPR 2011. pp. 449–456. IEEE (2011)
19. He, K., Zhang, X., Ren, S., Sun, J.: Deep residual learning for image recognition. In: Proceedings of the IEEE conference on computer vision and pattern recognition. pp. 770–778 (2016)

20. Heusel, M., Ramsauer, H., Unterthiner, T., Nessler, B., Hochreiter, S.: Gans trained by a two time-scale update rule converge to a local nash equilibrium. In: *Advances in neural information processing systems*. pp. 6626–6637 (2017)
21. Hui, T.W., Loy, C.C., Tang, X.: Depth map super-resolution by deep multi-scale guidance. In: *European conference on computer vision*. pp. 353–369. Springer (2016)
22. Johnson, J., Alahi, A., Fei-Fei, L.: Perceptual losses for real-time style transfer and super-resolution. In: *European conference on computer vision*. pp. 694–711. Springer (2016)
23. Karras, T., Aila, T., Laine, S., Lehtinen, J.: Progressive growing of gans for improved quality, stability, and variation. *arXiv preprint arXiv:1710.10196* (2017)
24. Karras, T., Laine, S., Aila, T.: A style-based generator architecture for generative adversarial networks. In: *Proceedings of the IEEE Conference on Computer Vision and Pattern Recognition*. pp. 4401–4410 (2019)
25. Karras, T., Laine, S., Aittala, M., Hellsten, J., Lehtinen, J., Aila, T.: Analyzing and improving the image quality of stylegan. *arXiv preprint arXiv:1912.04958* (2019)
26. Kim, J., Kwon Lee, J., Mu Lee, K.: Deeply-recursive convolutional network for image super-resolution. In: *Proceedings of the IEEE conference on computer vision and pattern recognition*. pp. 1637–1645 (2016)
27. Ledig, C., Theis, L., Huszár, F., Caballero, J., Cunningham, A., Acosta, A., Aitken, A., Tejani, A., Totz, J., Wang, Z., et al.: Photo-realistic single image super-resolution using a generative adversarial network. In: *Proceedings of the IEEE conference on computer vision and pattern recognition*. pp. 4681–4690 (2017)
28. Lee, C.H., Liu, Z., Wu, L., Luo, P.: Maskgan: Towards diverse and interactive facial image manipulation. *arXiv preprint arXiv:1907.11922* (2019)
29. Lee, C.H., Zhang, K., Lee, H.C., Cheng, C.W., Hsu, W.: Attribute augmented convolutional neural network for face hallucination. In: *Proceedings of the IEEE Conference on Computer Vision and Pattern Recognition Workshops*. pp. 721–729 (2018)
30. Li, M., Sun, Y., Zhang, Z., Xie, H., Yu, J.: Deep learning face hallucination via attributes transfer and enhancement. In: *2019 IEEE International Conference on Multimedia and Expo (ICME)*. pp. 604–609. IEEE (2019)
31. Li, X., Liu, M., Ye, Y., Zuo, W., Lin, L., Yang, R.: Learning warped guidance for blind face restoration. In: *Proceedings of the European Conference on Computer Vision (ECCV)*. pp. 272–289 (2018)
32. Liu, Z., Luo, P., Wang, X., Tang, X.: Deep learning face attributes in the wild. In: *Proceedings of International Conference on Computer Vision (ICCV)* (December 2015)
33. Ni, K.S., Nguyen, T.Q.: Image superresolution using support vector regression. *IEEE Transactions on Image Processing* **16**(6), 1596–1610 (2007)
34. Park, T., Liu, M.Y., Wang, T.C., Zhu, J.Y.: Semantic image synthesis with spatially-adaptive normalization. In: *Proceedings of the IEEE Conference on Computer Vision and Pattern Recognition*. pp. 2337–2346 (2019)
35. Riegler, G., Rüdter, M., Bischof, H.: Atgv-net: Accurate depth super-resolution. In: *European conference on computer vision*. pp. 268–284. Springer (2016)
36. Romero, A., Arbeláez, P., Van Gool, L., Timofte, R.: Smit: Stochastic multi-label image-to-image translation. In: *Proceedings of the IEEE International Conference on Computer Vision Workshops*. pp. 0–0 (2019)
37. Sajjadi, M.S., Scholkopf, B., Hirsch, M.: Enhancenet: Single image super-resolution through automated texture synthesis. In: *Proceedings of the IEEE International Conference on Computer Vision*. pp. 4491–4500 (2017)

38. Simonyan, K., Zisserman, A.: Very deep convolutional networks for large-scale image recognition. arXiv preprint arXiv:1409.1556 (2014)
39. Song, X., Dai, Y., Qin, X.: Deep depth super-resolution: Learning depth super-resolution using deep convolutional neural network. In: Asian conference on computer vision. pp. 360–376. Springer (2016)
40. Sun, J., Xu, Z., Shum, H.Y.: Image super-resolution using gradient profile prior. In: 2008 IEEE Conference on Computer Vision and Pattern Recognition. pp. 1–8. IEEE (2008)
41. Timofte, R., Agustsson, E., Van Gool, L., Yang, M.H., Zhang, L.: Ntire 2017 challenge on single image super-resolution: Methods and results. In: Proceedings of the IEEE conference on computer vision and pattern recognition workshops. pp. 114–125 (2017)
42. Timofte, R., De Smet, V., Van Gool, L.: A+: Adjusted anchored neighborhood regression for fast super-resolution. In: Asian conference on computer vision. pp. 111–126. Springer (2014)
43. Timofte, R., Gu, S., Wu, J., Van Gool, L.: Ntire 2018 challenge on single image super-resolution: Methods and results. In: Proceedings of the IEEE conference on computer vision and pattern recognition workshops. pp. 852–863 (2018)
44. Wang, Q., Tang, X., Shum, H.: Patch based blind image super resolution. In: Tenth IEEE International Conference on Computer Vision (ICCV’05) Volume 1. vol. 1, pp. 709–716. IEEE (2005)
45. Wang, T.C., Liu, M.Y., Zhu, J.Y., Tao, A., Kautz, J., Catanzaro, B.: High-resolution image synthesis and semantic manipulation with conditional gans. In: Proceedings of the IEEE conference on computer vision and pattern recognition. pp. 8798–8807 (2018)
46. Wang, X., Yu, K., Dong, C., Change Loy, C.: Recovering realistic texture in image super-resolution by deep spatial feature transform. In: Proceedings of the IEEE conference on computer vision and pattern recognition. pp. 606–615 (2018)
47. Wang, X., Yu, K., Wu, S., Gu, J., Liu, Y., Dong, C., Qiao, Y., Change Loy, C.: Esrgan: Enhanced super-resolution generative adversarial networks. In: Proceedings of the European Conference on Computer Vision (ECCV). pp. 0–0 (2018)
48. Wang, Z., Chen, J., Hoi, S.C.: Deep learning for image super-resolution: A survey. arXiv preprint arXiv:1902.06068 (2019)
49. Wang, Z., Bovik, A.C., Sheikh, H.R., Simoncelli, E.P.: Image quality assessment: from error visibility to structural similarity. *IEEE transactions on image processing* **13**(4), 600–612 (2004)
50. Yang, J., Wright, J., Huang, T.S., Ma, Y.: Image super-resolution via sparse representation. *IEEE transactions on image processing* **19**(11), 2861–2873 (2010)
51. Yu, F., Koltun, V.: Multi-scale context aggregation by dilated convolutions. In: International Conference on Learning Representations (ICLR) (2016)
52. Yu, F., Koltun, V., Funkhouser, T.: Dilated residual networks. In: Computer Vision and Pattern Recognition (CVPR) (2017)
53. Yu, X., Fernando, B., Ghanem, B., Porikli, F., Hartley, R.: Face super-resolution guided by facial component heatmaps. In: Proceedings of the European Conference on Computer Vision (ECCV). pp. 217–233 (2018)
54. Yu, X., Fernando, B., Hartley, R., Porikli, F.: Super-resolving very low-resolution face images with supplementary attributes. In: Proceedings of the IEEE Conference on Computer Vision and Pattern Recognition. pp. 908–917 (2018)
55. Zhang, H., Yang, J., Zhang, Y., Huang, T.S.: Non-local kernel regression for image and video restoration. In: European Conference on Computer Vision. pp. 566–579. Springer (2010)

56. Zhang, R., Isola, P., Efros, A.A., Shechtman, E., Wang, O.: The unreasonable effectiveness of deep features as a perceptual metric. In: CVPR (2018)
57. Zhu, P., Abdal, R., Qin, Y., Wonka, P.: Sean: Image synthesis with semantic region-adaptive normalization. arXiv preprint arXiv:1911.12861 (2019)

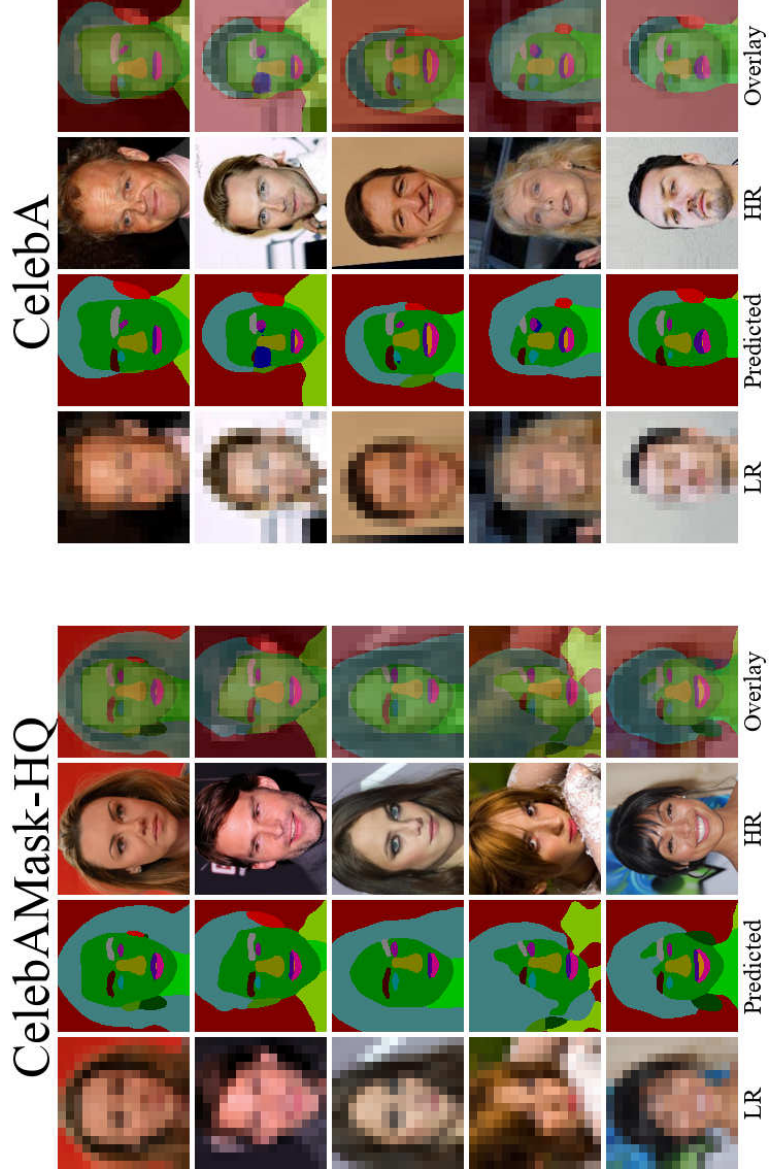


Fig. 2. Semantic Segmentation Results. We predict a high-resolution semantic mask (resolution 512×512 for CelebAMask-HQ and 128×128 for CelebA) from a low-resolution image (16×16). Columns three and five show the high-resolution image and column four and eight an overlay for a better comparison. The images are random samples from the test set

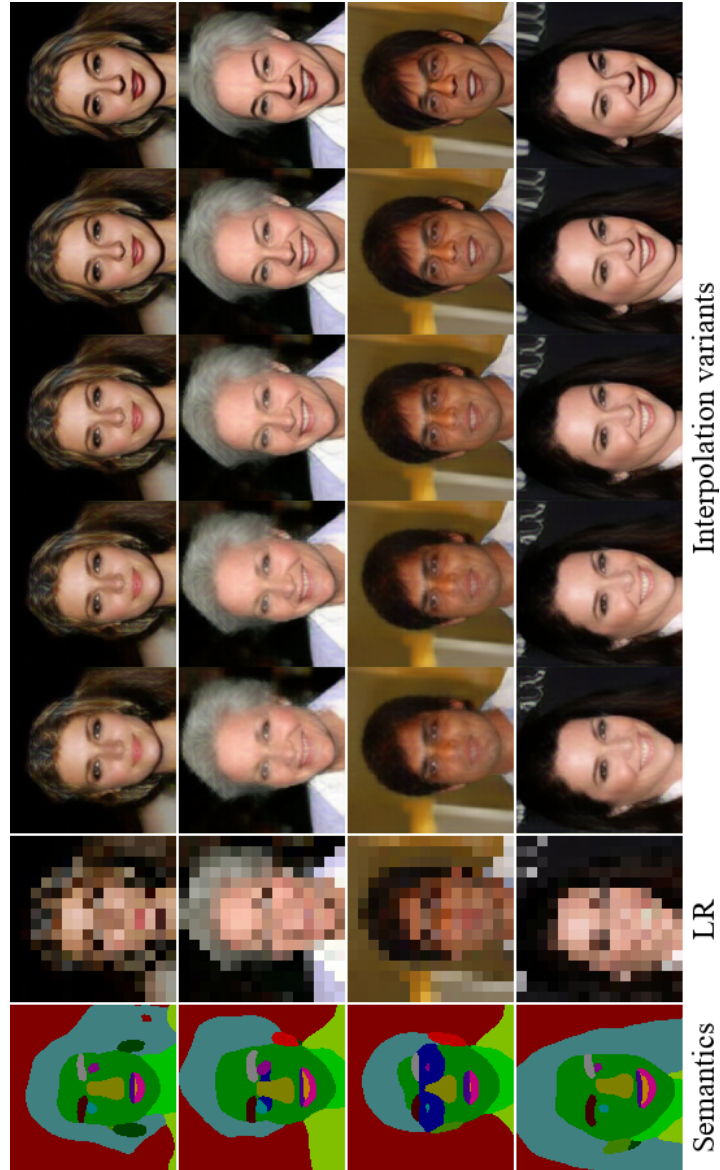


Fig. 3. Exploring Solutions by Walking the Latent Style Space (1). We predict the style from the low-resolution image (LR) and generate five smoothly varying solutions. The middle image (column five) uses the predicted style matrix without any changes. For the images on the either side, we subtract (left), respectively add (right) a linearly interpolated δ to the style matrix. We apply the same $\delta = 0.15$ to all regions

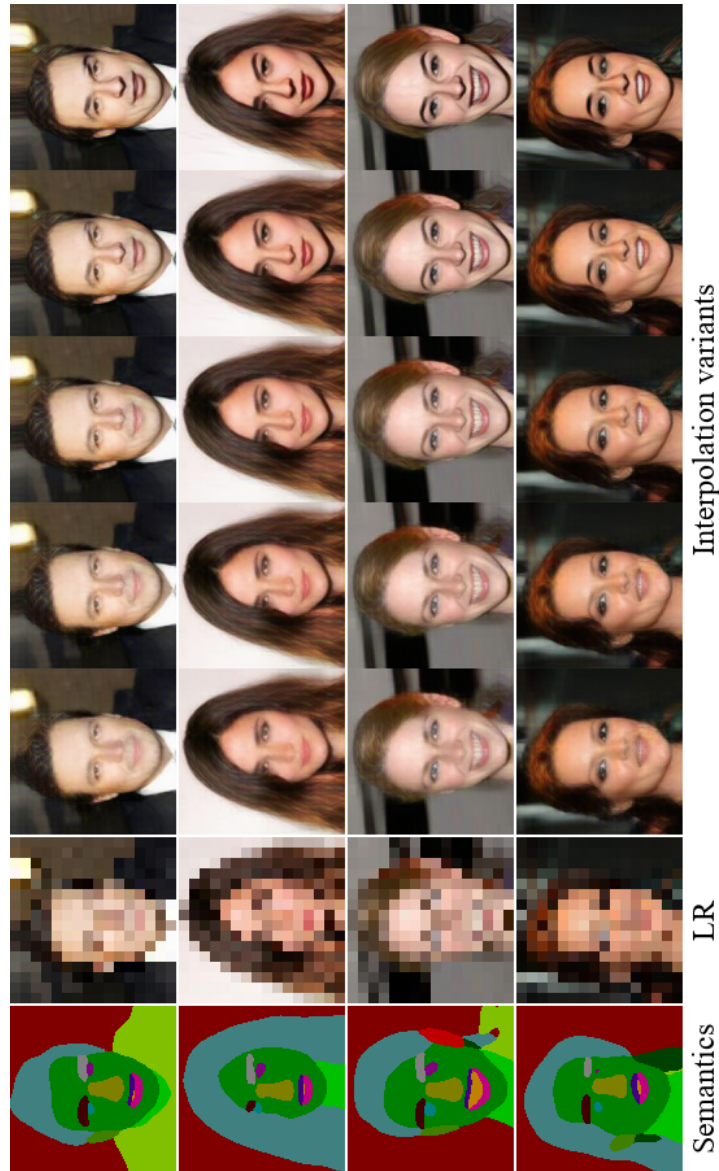


Fig. 4. Exploring Solutions by Walking the Latent Style Space (2). This visualization extends Figure 3 with more examples. Note, how large regions, like hair, are very consistent, and small regions, such as lips and eyebrows, vary a lot more. The reason is that the low-resolution input image provide the generator with a strong for larger regions. In contrast, the generator has more freedom for small, uncertain regions and relies more on the style matrix to provide appearance information. This behaviour is wanted because it allows to preserve identities, but leaves the possibility to explore uncertain areas

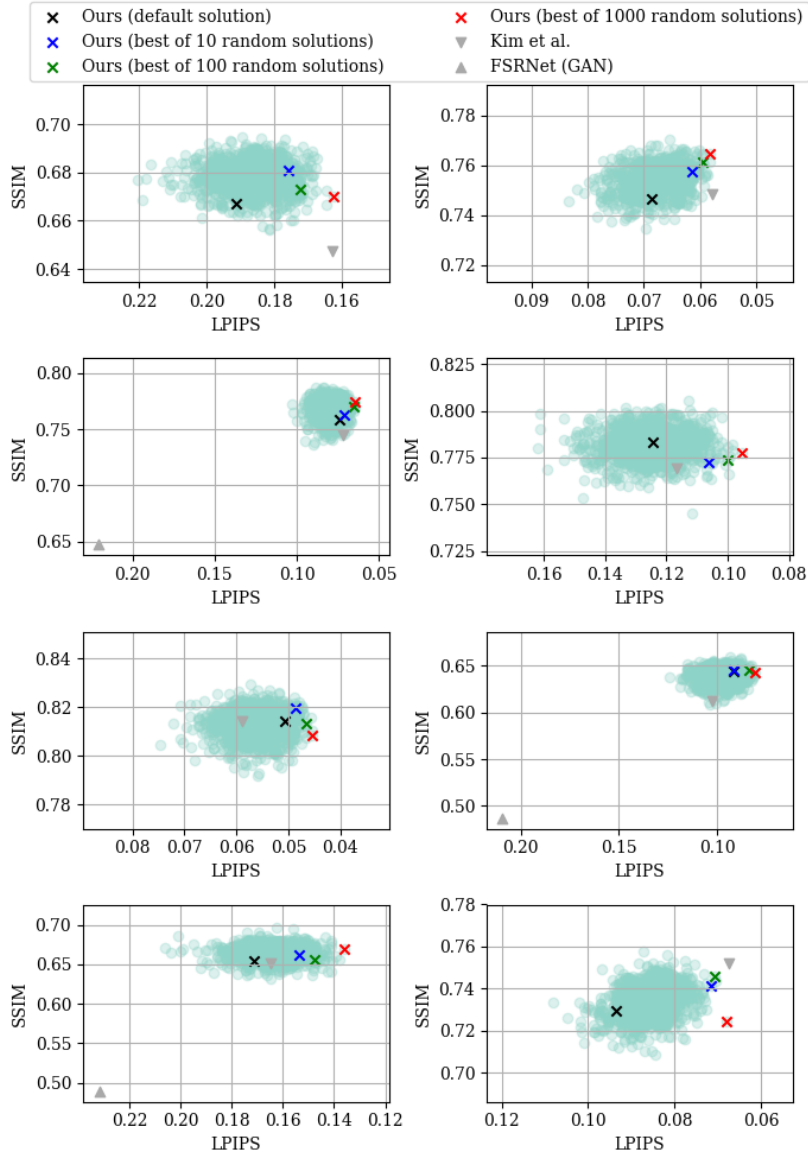


Fig. 5. Explorative Oracle Selection for Perceptual Quality. We choose 12 random test images (one image per plot) and sample many possible outcomes from our model (illustrated as point clouds). We now pick 1, 10, 100 and 1,000 random solutions and mark best-scoring image (in terms of LPIPS [56]) with a cross. Figure 6 shows a similar plot for the image with highest SSIM [49]. While Kim et al. [11] and FSRNet [9] predict a single deterministic solution, *DeepSEE* can generate an infinite number of solutions and enables the user to pick the most desirable outcome

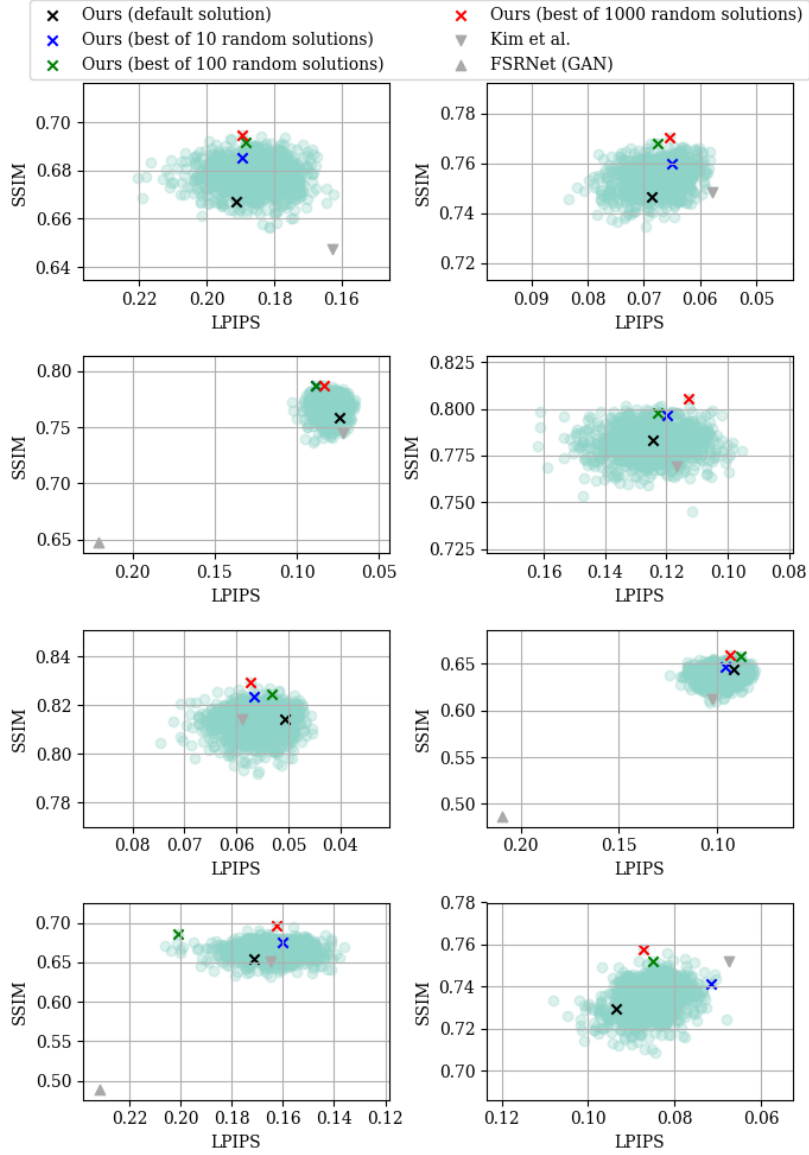


Fig. 6. Explorative Oracle Selection for Image Fidelity. We apply the same process as in Figure 5, but sample with respect to highest SSIM [49]. In most cases, the best out of 10 random solutions is already very close to the best sample overall

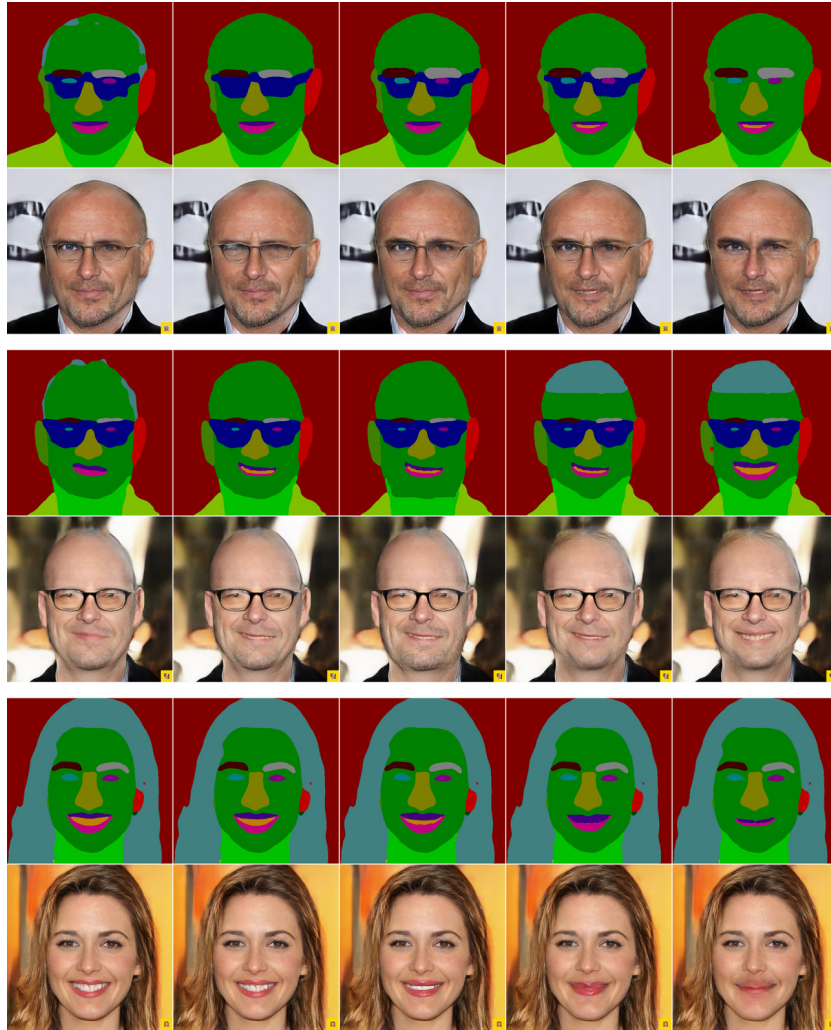


Fig. 7. Multiple Continuous Semantic Manipulations We show three examples, where we modify the semantic mask multiple times. For each sample, the first semantic mask is the original prediction and the subsequent masks have been modified. In the first example, we manipulate eyes, mouth and glasses. In the second example, we also add some hair to the top of the bold head. The third example shows a smooth transition from an open to a closed mouth

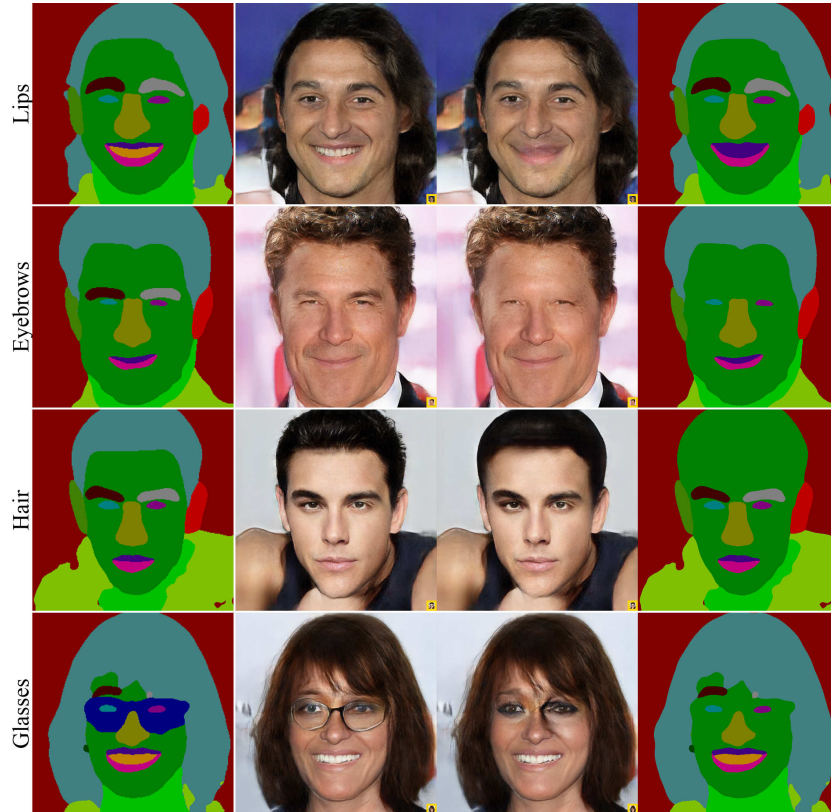


Fig. 8. Semantic Manipulations for $32\times$ Upscaling In the top row, we replace the mouth region with lips, which yields a closed mouth. The second row replaces eyebrows with skin, making them disappear. The bottom two rows show cases where the manipulated semantic mask is inconsistent with the low-resolution input. For example, when replacing the annotations for hair with skin, the model still renders a dark region, resembling smooth hair. In the last row, we remove glasses, which produces a strong makeup around the eye-region. Please read 3.2 for a discussion



Fig. 9. Disentangled Manipulations for the *Independent* Model. We show multiple $8\times$ upscaled variants, where we modify the style input for the highlighted semantic region. We observe a high identity consistency across different variants, but visible changes in the selected semantic regions. For this figure, we focus on high-frequency details, which are better visible in the small, so please zoom in for better view

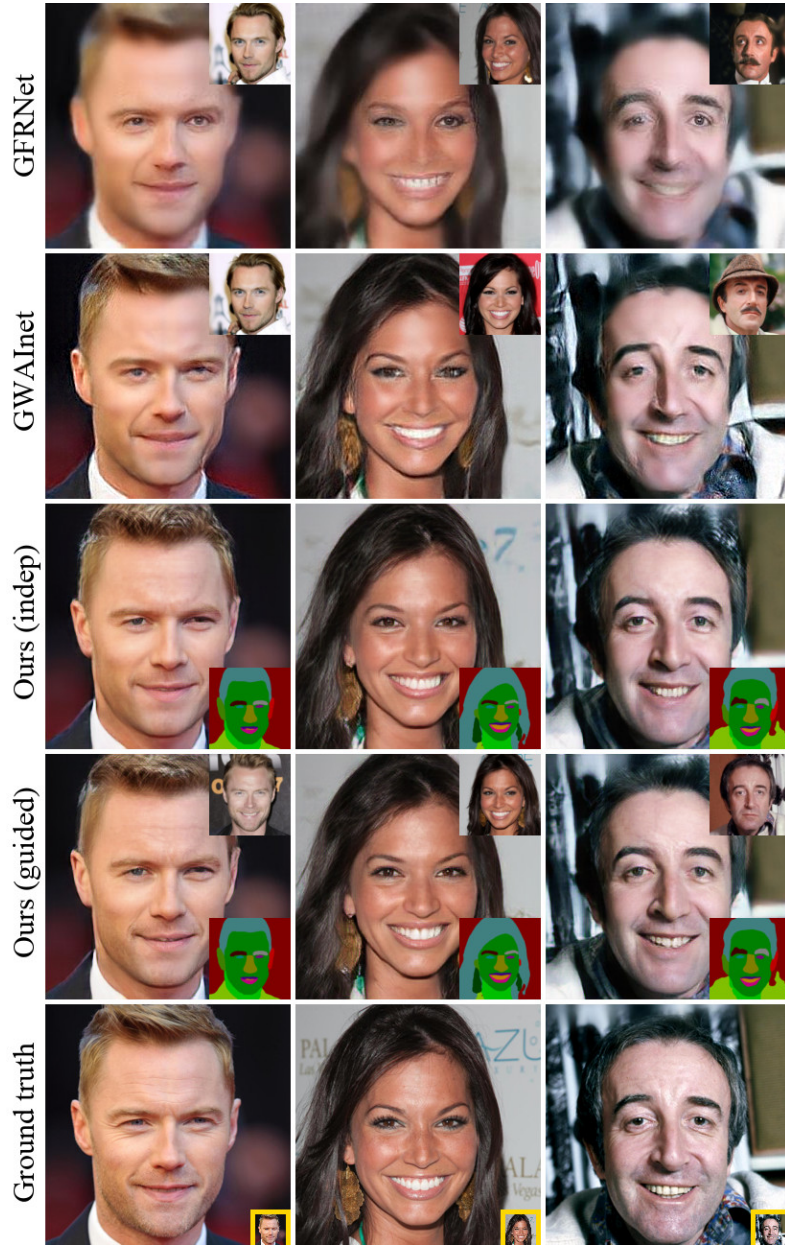


Fig. 10. Additional Comparison to Related Work (1). We visually compare to related models (GFRNet [31] and GWAInet [12]) for upscaling $8\times$. The small image in the top right corners shows a random image from the same person, used as guiding image. For our models, we show the predicted segmentation mask in the bottom right corner. The last row shows the ground truth with the low-resolution input image in the bottom right. Please zoom in for better view

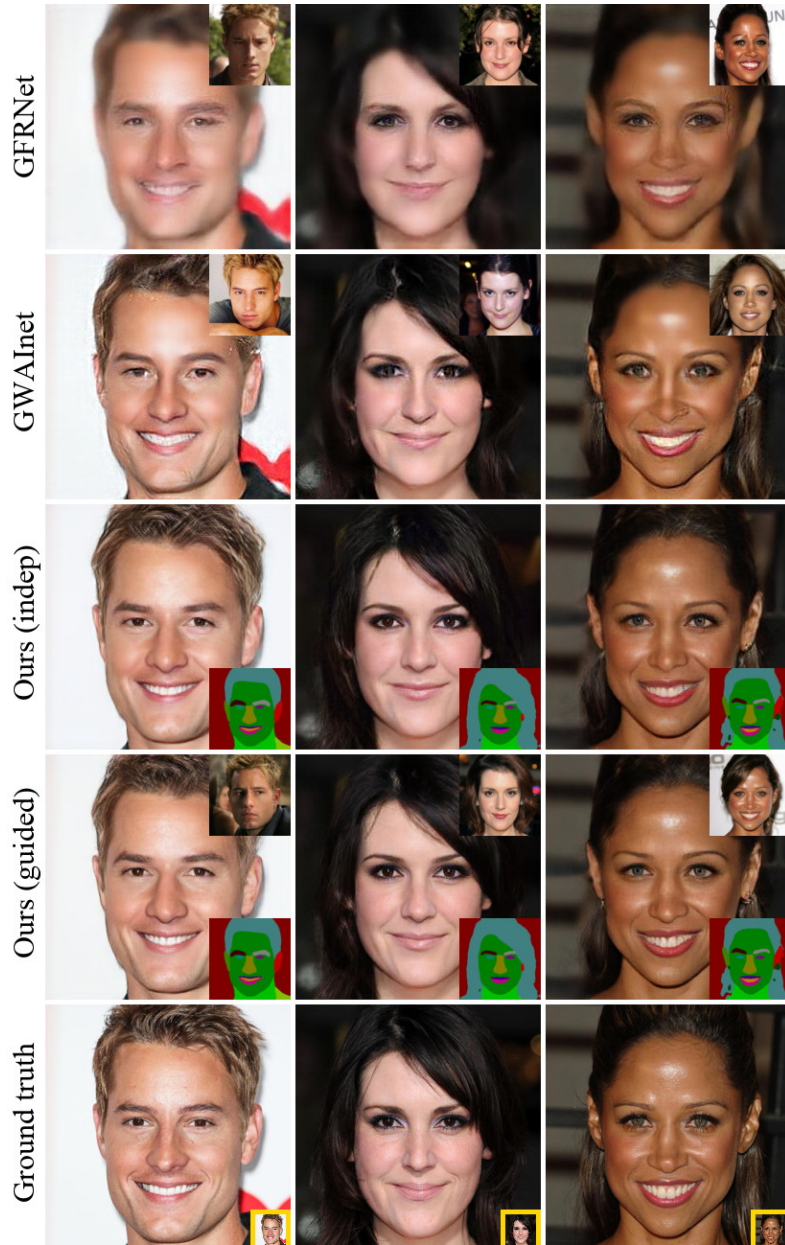


Fig. 11. Additional Comparison to Related Work (2). We extend Figure 10 with additional examples. Please zoom in for better view

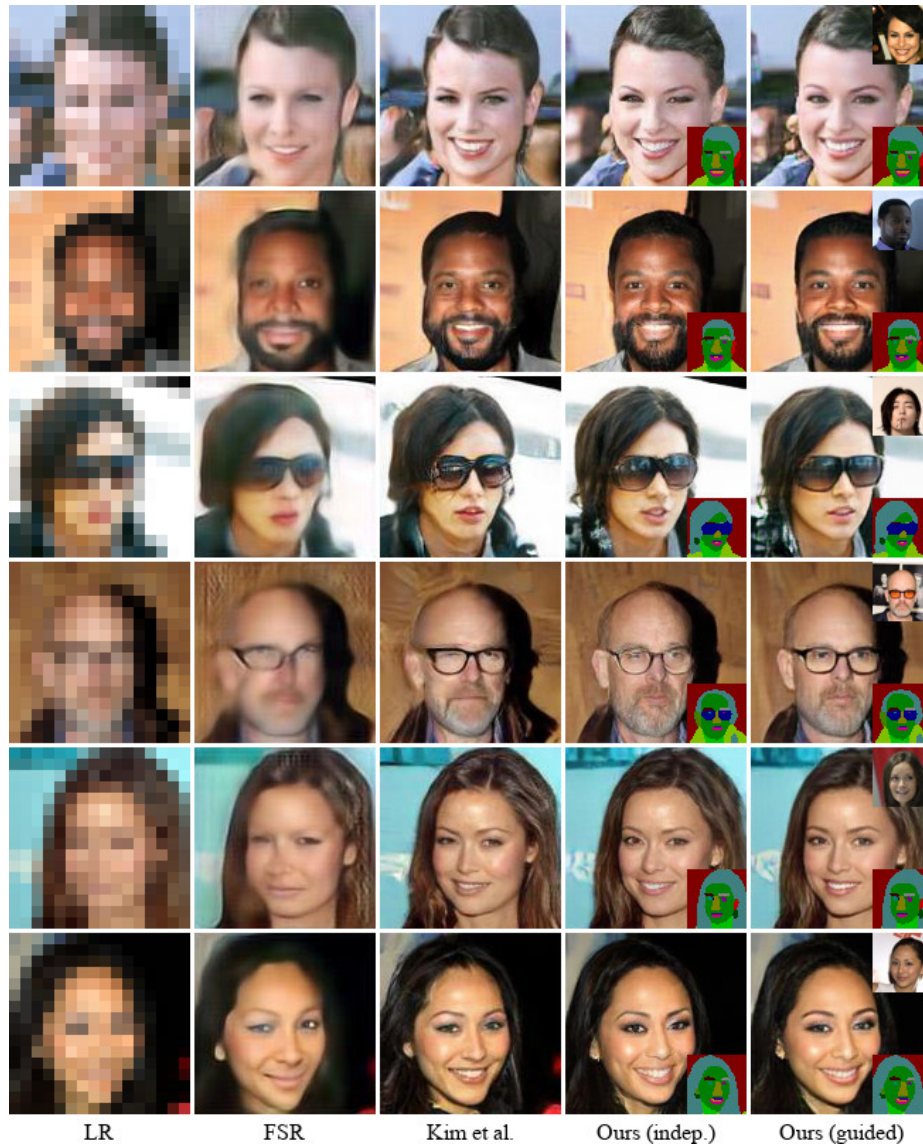


Fig. 12. Comparison with Methods Guided by Facial Landmarks. We compare to FSR [9] and Kim *et al.* [11] with upscaling factor $8\times$, starting at 16×16 . For the *guided* model, the small image in the top right shows the reference image. Our method produces more realistic outputs, in particular for difficult regions, like hair, glasses or earrings



Fig. 13. Extreme Super-resolution (1). This figure shows a larger version of the left example in Figure 6 in the main paper. The yellow image in the bottom right is the low-resolution input image, which is upscaled $32\times$

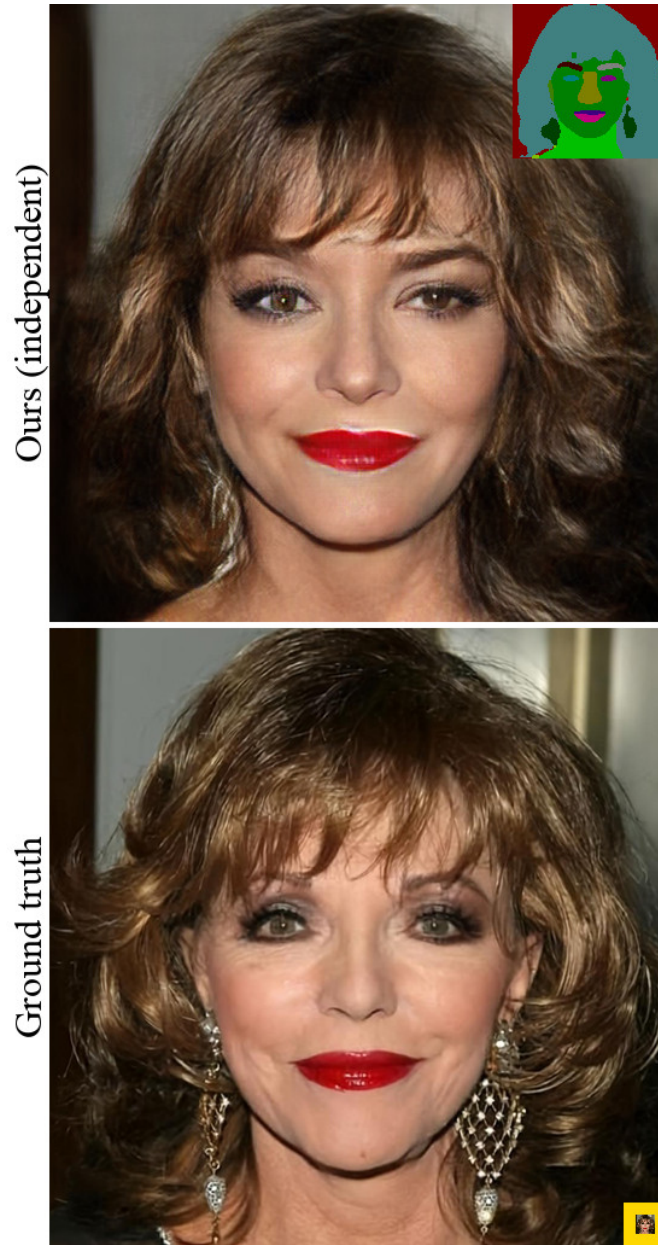


Fig. 14. Extreme Super-resolution (2). This figure shows a larger version of the right example in Figure 6 in the main paper. The style encoder did not recognize the low-resolution image as a middle-aged woman, and instead produces the style code for a young woman. We discuss this observation in the main paper in more detail



Fig. 15. Extreme Super-resolution (3). Note how in this case the model generated a closed mouth. While a deterministic model would fail to generate the correct solution, a user could now manipulate the segmentation mask to produce the correct version with an open mouth